

Abrupt ice-age shifts in southern westerly winds and Antarctic climate forced from the north

Christo Buizert^{1*}, Michael Sigl^{2,14}, Mirko Severi³, Bradley R. Markle⁴, Justin J. Wettstein^{1,5}, Joseph R. McConnell⁶, Joel B. Pedro^{7,8}, Harald Sodemann⁵, Kumiko Goto-Azuma⁹, Kenji Kawamura⁹, Shuji Fujita⁹, Hideaki Motoyama⁹, Motohiro Hirabayashi⁹, Ryu Uemura¹⁰, Barbara Stenni¹¹, Frédéric Parrenin¹², Feng He^{1,13}, T. J. Fudge⁴ & Eric J. Steig⁴

The mid-latitude westerly winds of the Southern Hemisphere play a central role in the global climate system via Southern Ocean upwelling¹, carbon exchange with the deep ocean², Agulhas leakage (transport of Indian Ocean waters into the Atlantic)³ and possibly Antarctic ice-sheet stability⁴. Meridional shifts of the Southern Hemisphere westerly winds have been hypothesized to occur^{5,6} in parallel with the well-documented shifts of the intertropical convergence zone⁷ in response to Dansgaard-Oeschger (DO) events— abrupt North Atlantic climate change events of the last ice age. Shifting moisture pathways to West Antarctica⁸ are consistent with this view but may represent a Pacific teleconnection pattern forced from the tropics⁹. The full response of the Southern Hemisphere atmospheric circulation to the DO cycle and its impact on Antarctic temperature remain unclear¹⁰. Here we use five ice cores synchronized via volcanic markers to show that the Antarctic temperature response to the DO cycle can be understood as the superposition of two modes: a spatially

homogeneous oceanic ‘bipolar seesaw’ mode that lags behind Northern Hemisphere climate by about 200 years, and a spatially heterogeneous atmospheric mode that is synchronous with abrupt events in the Northern Hemisphere. Temperature anomalies of the atmospheric mode are similar to those associated with present-day Southern Annular Mode variability, rather than the Pacific–South American pattern. Moreover, deuterium-excess records suggest a zonally coherent migration of the Southern Hemisphere westerly winds over all ocean basins in phase with Northern Hemisphere climate. Our work provides a simple conceptual framework for understanding circum-Antarctic temperature variations forced by abrupt Northern Hemisphere climate change. We provide observational evidence of abrupt shifts in the Southern Hemisphere westerly winds, which have previously documented^{1–3} ramifications for global ocean circulation and atmospheric carbon dioxide. These coupled changes highlight the necessity of a global, rather than a purely North Atlantic, perspective on the DO cycle.

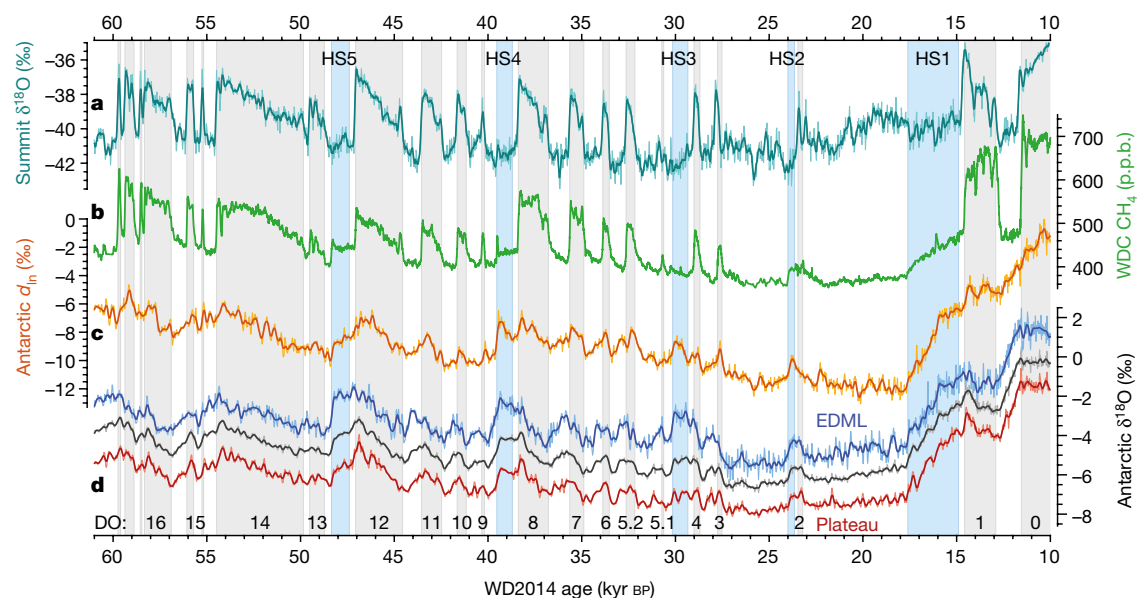


Fig. 1 | Records of abrupt glacial climate variability. **a**, Ice-core $\delta^{18}\text{O}$ (average of GISP2 and GRIP²⁸) at the Greenland summit. **b**, WDC methane²⁹, p.p.b., parts per 10^9 . **c**, Antarctic five-core (EDC, EDML, TAL and DF) average d_{in} anomaly. **d**, Antarctic $\delta^{18}\text{O}$ anomaly at EDML (blue), the Antarctic Plateau (average of DF and EDC; red) and five-core average (black). All records are synchronized to WD2014 chronology; Antarctic data are shown as anomalies relative to the present, with the EDML and

Antarctic Plateau lines offset by +1.4‰ and –1.3‰, respectively, for clarity. DO interstadial periods are marked in grey and numbered, and Heinrich stadials (HS1–HS5) are marked in blue. Isotope ratios are on the VSMOW (Vienna Standard Mean Ocean Water) scale. Thin lines show records at the original resolution (ranging from about 5 to about 50 yr), and thick lines are a moving average (with a 300-yr and 150-yr window for Antarctic and Greenland data, respectively).

¹College of Earth, Ocean and Atmospheric Sciences, Oregon State University, Corvallis, OR, USA. ²Laboratory of Environmental Chemistry, Paul Scherrer Institute, Villigen, Switzerland. ³Department of Chemistry ‘Ugo Schiff’, University of Florence, Florence, Italy. ⁴Department of Earth and Space Science, University of Washington, Seattle, WA, USA. ⁵Geophysical Institute and Bjerknes Centre for Climate Research, University of Bergen, Bergen, Norway. ⁶Desert Research Institute, Nevada System of Higher Education, Reno, NV, USA. ⁷Centre for Ice and Climate, Niels Bohr Institute, University of Copenhagen, Copenhagen, Denmark. ⁸Antarctic Climate & Ecosystems Cooperative Research Centre, University of Tasmania, Hobart, Tasmania, Australia. ⁹National Institute for Polar Research, Tachikawa, Tokyo, Japan. ¹⁰Department of Chemistry, Biology and Marine Science, University of the Ryukyus, Okinawa, Japan. ¹¹Department of Environmental Sciences, Informatics and Statistics, Ca’ Foscari University of Venice, Venice, Italy. ¹²Université Grenoble Alpes, CNRS, IRD, IGE, Grenoble, France. ¹³Center for Climatic Research, Nelson Institute for Environmental Studies, University of Wisconsin-Madison, Madison, WI, USA. ¹⁴Present address: Oeschger Centre for Climate Change Research, University of Bern, Bern, Switzerland. *e-mail: buizertc@oregonstate.edu

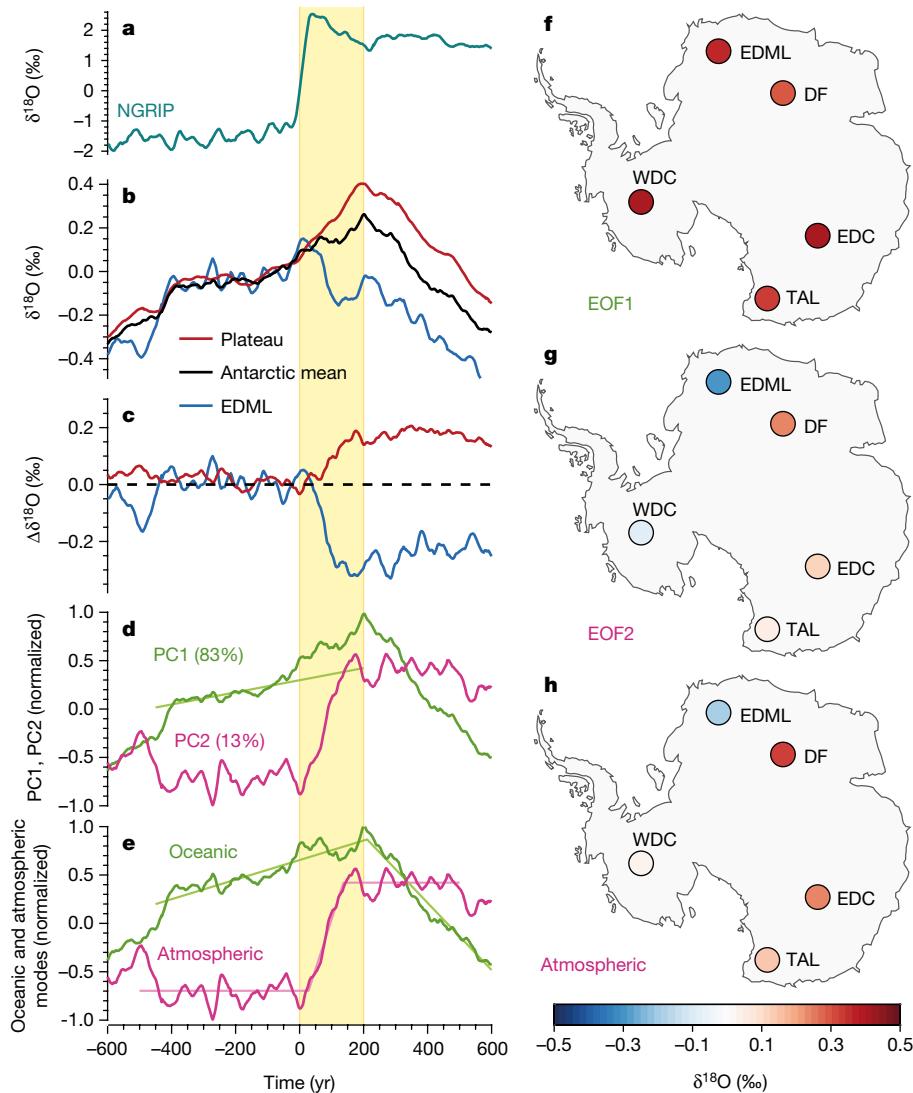


Fig. 2 | Antarctic climate response to DO warming. **a**, Stack of North Greenland Ice Core Project (NGRIP) $\delta^{18}\text{O}$ records. **b**, Stack of Antarctic $\delta^{18}\text{O}$ records at the indicated locations, with ‘Plateau’ representing the average of DF and EDC. **c**, As in **b**, but with the five-core mean subtracted. **d**, First two principal components of the Antarctic $\delta^{18}\text{O}$ stacks (1,500-yr window), with the percentage of variance provided (PC2 is offset by -0.15 for clarity). PC1 is strongly correlated ($r = 0.998$) to the Antarctic mean. A linear fit to PC1 (interval from $t = -400$ yr to $t = 0$) is shown to highlight the response around $t = 0$. **e**, Proposed oceanic and atmospheric modes,

obtained using rotated principal component vectors (Methods). Fits from change-point analysis (Methods) are also shown. The oceanic mode responds at $t = 211 \pm 42$ yr and the atmospheric mode at $t = 28 \pm 40$ yr (1σ bounds; Extended Data Table 1). Curves in **d** and **e** are normalized to have $2\sigma = 1$. **f**, **g**, Empirical orthogonal functions EOF1 and EOF2 associated with PC1 and PC2 in **d**, scaled to $\delta^{18}\text{O}$ units (‰). **h**, Spatial pattern associated with the atmospheric mode shown in **e**, scaled to $\delta^{18}\text{O}$ units (‰). Isotope ratios are on the VSMOW scale.

During the glacial DO cycle, abrupt variations in northward heat transport by the Atlantic meridional overturning circulation (AMOC) affect Greenland and Antarctic temperatures oppositely (Fig. 1), via an oceanic teleconnection called the bipolar seesaw^{6,11}. Antarctica warms during Greenland cold phases (stadials) and cools during Greenland warm phases (interstadials), with the gradual nature of Antarctic climate change reflecting buffering by a large heat reservoir¹¹—probably the global ocean interior⁶. The DO cycle also affects atmospheric circulation; the intertropical convergence zone shifts southwards during stadials and northwards during interstadials⁷. General circulation model (GCM) simulations suggest parallel shifts of the Southern Hemisphere westerly winds (westerlies)^{5,6,12}, but the available observational evidence (a deuterium-excess record from West Antarctica⁸) cannot distinguish between such shifts and Pacific-only teleconnections⁹. Furthermore, the impact of the atmospheric circulation changes on Antarctic climate remains unknown, and models are inconclusive on this question^{10,13}.

We use water stable isotope ratios, a proxy for site temperature¹⁴, from five Antarctic ice cores: WAIS (West Antarctic Ice Sheet) Divide (WDC),

EPICA (European Project for Ice Coring in Antarctica) Dronning Maud Land (EDML), EPICA Dome C (EDC), Dome Fuji (DF) and Talos Dome (TAL). WDC is synchronized to Greenland ice cores at high precision via atmospheric methane (Fig. 1a, b)¹⁵; here we synchronize WDC to the other cores in the interval 10–57 kyr before present (BP) using volcanic markers (Methods; Extended Data Fig. 1), greatly improving our ability to study the timing of regional Antarctic climate variations relative to Greenland. We investigate the Antarctic response to DO events using a stacking technique¹⁵ in which 19 individual events are aligned at the midpoint of their abrupt methane transition in WDC and averaged to obtain the shared climatic signal (Methods).

Antarctica cools in response to DO warming (Fig. 2a, b), consistent with the bipolar seesaw theory^{6,11}. In the Antarctic mean $\delta^{18}\text{O}$ stack (where $\delta^{18}\text{O}$ represents the $^{18}\text{O}/^{16}\text{O}$ composition), the cooling onset occurs about two centuries after the abrupt Northern Hemisphere event, providing validation of earlier results from West Antarctica¹⁵. There is a spatial pattern to the Antarctic response, however. A step-like divergence from the mean signal is seen around $t \approx 0$ yr (that is,

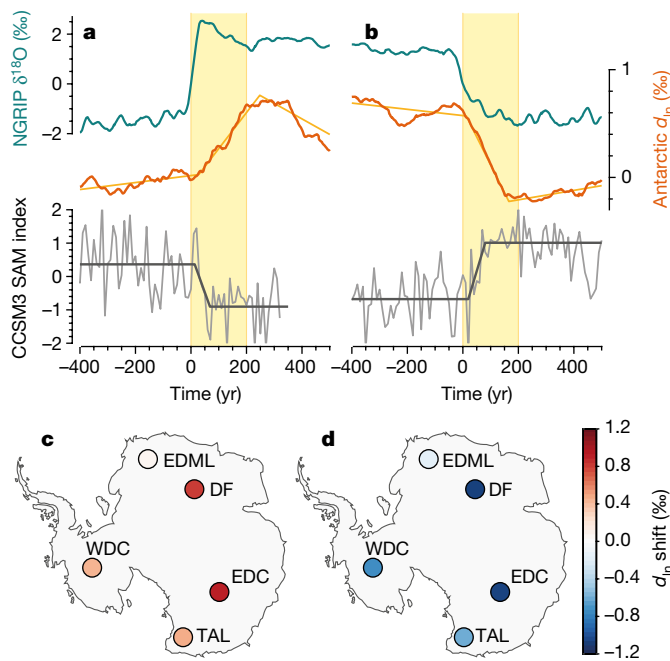


Fig. 3 | Deuterium excess and the Southern Hemisphere westerlies. **a**, DO warming. Shown are data from the NGRIP $\delta^{18}\text{O}$ stack (turquoise); five-core average Antarctic d_{in} stack (orange, with fit from change-point analysis; see Extended Data Table 1); the SAM index (here the leading principal component of sea-level pressure variability south of 20°S) following a freshwater-forced AMOC perturbation in CCSM3 (Community Climate System Model version 3) simulations (grey, with fit from change-point analysis; see Extended Data Table 1). **b**, As in **a**, but for DO cooling. **c**, Magnitude of Antarctic d_{in} response to DO warming. The weak d_{in} trend before and after the abrupt jump probably reflects the SST of Southern Hemisphere vapour source waters following the thermal bipolar seesaw^{8,11}. **d**, As in **c**, but for DO cooling. Isotope ratios are on the VSMOW scale.

synchronous with Northern Hemisphere climate), with the interior East Antarctic Plateau sites (DF and EDC) warming and EDML cooling (Fig. 2c). This instantaneous warming over the plateau is particularly pronounced at DO events 1, 8, 12 and 14 (Fig. 1d, red curve).

Using principal component analysis (PCA; see Methods), we find that two modes of variability explain more than 96% of signal variance in the five stacked records (Fig. 2d). The first principal component (PC1; 83% of variance explained) has the triangular shape of the Antarctic isotope maximum events—the classic thermal bipolar seesaw signal¹¹—with a spatially homogeneous expression (Fig. 2f). The two-century lag behind Greenland warming identifies PC1 as an ocean-propagated response¹⁵.

The second principal component (PC2; 13% of variance explained) is a step-like function with a heterogeneous spatial pattern (Fig. 2g). This mode is very different from the bipolar seesaw. The PC2 response is synchronous with Northern Hemisphere warming within precision (28 ± 40 year lag, 1σ bounds; see Methods); this timing, as well as additional evidence presented below, suggests that this mode represents an atmospheric teleconnection. The PCA does not necessarily separate physical processes. We assume two underlying teleconnections: oceanic (two-century lag) and atmospheric (synchronous). Some amount of each process is included in PC1, as evident by some immediate warming around $t = 0$. We perform a rotation of the PCA vectors (Methods) to isolate the ‘purely’ oceanic and atmospheric responses (Fig. 2e). The associated estimate of the atmospherically forced temperature anomaly (Fig. 2h) is cooling at EDML, warming at DF, EDC and TAL, and a negligible response at WDC; this pattern is robustly reproduced using different methods (Extended Data Fig. 6). The magnitude of the Antarctic atmospheric response is roughly proportional to the $\delta^{18}\text{O}$ perturbation in Greenland ice cores (Extended Data Fig. 4).

The Antarctic response to DO cooling is qualitatively similar to the DO warming case. The ocean seesaw warming response is delayed by 226 ± 44 yr and the spatial pattern of the empirical orthogonal function EOF2 has the opposite sign—that is, additional warming at EDML and cooling on the interior of the East Antarctic Plateau (Extended Data Fig. 7). The atmospheric signal over Antarctica is much weaker for the DO cooling case, with PC2 explaining only 9% of variance. This difference is likely due to the fact that DO warmings are more abrupt and of larger magnitude than DO coolings.

To better understand the atmospheric mode, we turn to deuterium excess (d), a proxy for vapour source conditions¹⁶ commonly used to identify changes in atmospheric circulation and vapour transport pathways^{8,17,18}. In isotope-enabled GCM simulations, Antarctic d is anti-correlated with the Southern Annular Mode (SAM) index^{8,19}. This anti-correlation can be understood conceptually: when the Southern Hemisphere westerlies are displaced equatorwards (negative SAM phase), Antarctic moisture will originate from further north, where sea surface temperature (SST) is higher and relative humidity is lower (Extended Data Fig. 8b), both of which act to make d more positive¹⁶. We use the logarithmic definition of deuterium excess (d_{in}), which preserves isotopic moisture source information better than the linear definition^{8,20}.

The Antarctic mean d_{in} response (Fig. 3a, b) lags behind Northern Hemisphere climate by 8 ± 48 yr for DO warming and 9 ± 42 yr for DO cooling, consistent with previous results for WDC⁸. The observed d_{in} response is consistent with a shift in the meridional position of the Southern Hemisphere westerly winds and vapour origin, such that they move equatorwards in response to Northern Hemisphere warming and polewards in response to cooling. The timing suggests propagation to high latitudes of the Southern Hemisphere via an atmospheric teleconnection. The d_{in} response is largest for the interior Plateau sites (DF and EDC), possibly because their vapour source areas are more distant from confounding local effects such as the sea–ice edge²¹. The response is weak or absent at EDML, possibly because the variability of Southern Hemisphere westerlies is relatively weak in the Atlantic sector (Extended Data Fig. 9), or because of regional effects, such as wind-driven changes to the sea ice, gyre circulation or Weddell Sea deep convection²². Critically, the four cores that do show a clear d_{in} response collectively sample water vapour from all ocean basins (Extended Data Fig. 8a), suggesting that the changes to Southern Hemisphere atmospheric circulation are zonally coherent and involve all ocean basins (rather than just the Pacific basin, as demonstrated previously with WDC).

Figure 4a compares the two independent signals that we attribute to a change in atmospheric circulation: PC2 of the $\delta^{18}\text{O}$ response and the Antarctic mean d_{in} response. Their time evolution is nearly identical, suggesting that they are distinct but consistent manifestations of the atmospheric circulation change. The SAM and Pacific–South American (PSA) pattern are the leading modes of large-scale Southern Hemisphere atmospheric variability with strong influence on Antarctic temperature^{9,23}. We focus our analysis on East Antarctica, where we infer the largest response. The SAM (Fig. 4b) clearly impacts East Antarctic surface air temperature (SAT) strongly (correlation $|r|$ up to 0.65) and with the correct sign to explain the warming seen at EDC, DF and TAL. East Antarctic warming is seen for a more negative SAM index, driven primarily by anomalous atmospheric heat advection²⁴ (the observed cooling at EDML is discussed below). The PSA (Fig. 4c), on the other hand, is not meaningfully correlated with the SAT at the East Antarctic sites ($|r| \leq 0.15$). We further create a synthetic index that is the projection of the atmospheric loadings (Fig. 2h) onto the SAT anomaly inferred from the reanalysis at the core locations (Methods). The patterns in the SAT and the geopotential height associated with this index (Fig. 4d) closely resemble those of the SAM, with warming in East Antarctica and roughly annular geopotential height anomalies.

These tests suggest that the SAM is the closest present-day analogue to the temperature response that we identify in the ice-core record, corroborating our independent evidence from the d_{in} data. Although

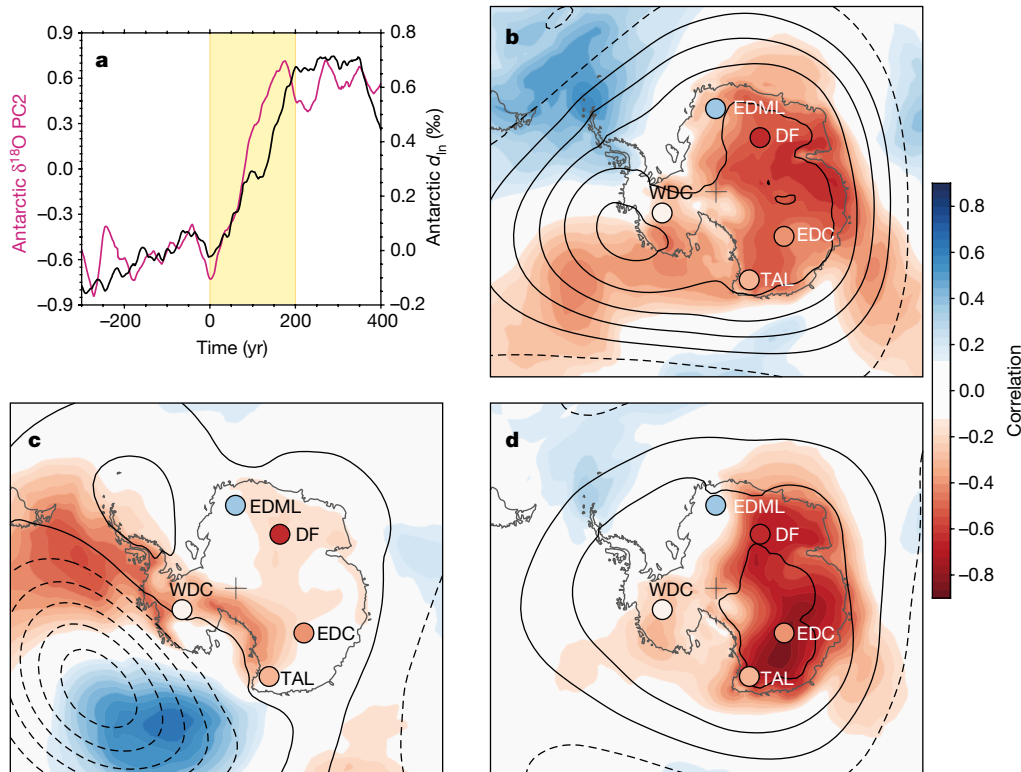


Fig. 4 | Attribution of the atmospheric mode of Antarctic temperature variability. **a**, Comparison of the principal component PC2 of the five Antarctic $\delta^{18}\text{O}$ stacks shown in Fig. 2d (pink; left axis) with the Antarctic mean d_{in} stack shown in Fig. 3a (black; right axis). Isotope ratios are on the VSMOW scale. **b**, Correlation between a standardized monthly SAM index and the SAT (2-m temperature) in ERA-Interim³⁰ for 1979–2017 (shading; colour bar on the right) with superimposed 850-hPa geopotential height regressions (10-m contours) and the ice-core atmospheric temperature

mode from Fig. 2h (circles; scale bar from Fig. 2). We note that regions of anti-correlation are coloured red (that is, warming in response to a negative SAM shift). **c**, As in **b**, but for a standardized PSA index. The SAM and PSA are taken to be the PC1 and PC2 principal components of the 850-hPa geopotential height field south of 20° S, respectively. **d**, As in **b**, but for a synthetic index of the atmospheric mode created by regressing ERA-Interim SAT anomalies at the ice-core sites onto the coefficients in Fig. 2h (Methods).

the PSA pattern may have been active during the DO cycle, it does not dominate the Antarctic response.

Our observation-based inferences on the timing and sign of changes to the Southern Hemisphere westerlies and the SAM are consistent with coupled atmosphere–ocean GCM simulations in which AMOC transitions are induced by North Atlantic freshwater forcing^{6,12,25}. Such model simulations show a positive shift in the SAM index in response to AMOC shutdown and vice versa (Fig. 3a, b); this shift is synchronous with the applied forcing within uncertainty (Extended Data Table 1). Our observed atmospheric response is more gradual than the model-simulated SAM shift, possibly because of the (multi-decadal) data resolution in some cores and the fact that the d_{in} signal is integrated over a large moisture source area extending to 20° S.

Next, we address differences between the ice-core data and the modern-day correlation pattern (Fig. 4b), most notably at EDML. The reanalysis correlation pattern captures the SAT response to monthly internal SAM variability, representing atmospheric heat advection anomalies²⁴. The ice cores, on the other hand, record the response to a persistent long-term shift in the SAM^{13,26}, driving changes in SST, stratification and sea ice extent^{22,26}. We speculate that on longer timescales the oceanic influence of the Weddell Sea drives the cooling at EDML owing to, for example, enhanced sea ice cover²² and stratification and a weakening of the wind-driven Weddell Gyre. The negligible warming response at WDC is consistent with the relatively weak influence of the SAM in West Antarctica seen in the monthly reanalysis (Fig. 4b). Our observations may help to constrain the long-term response to a persistent SAM shift, on which GCMs disagree¹⁵.

Lastly, we want to highlight additional structure in the Antarctic $\delta^{18}\text{O}$ stacks that is currently not part of scientific discourse on interhemispheric climate coupling. Most notably, Antarctic warming appears to

slow down around $t = -400$ yr (Fig. 2b), forming a secondary change point that precedes the abrupt DO warming events²⁷. Likewise, the rate of Antarctic cooling appears to increase 200 years before the abrupt DO cooling events (Extended Data Fig. 7b). These secondary change points are subtler than the ones analysed in this work, have no apparent corresponding features in Antarctic d_{in} or Greenland climate and remain unexplained.

In conclusion, our results show that Antarctica is influenced by abrupt changes in Northern Hemisphere climate on two distinct timescales, representing a slow oceanic and a fast atmospheric teleconnection. In particular, we provide observational evidence for zonally coherent meridional shifts in the Southern Hemisphere westerly winds in phase with Greenland DO events and their impact on Antarctic temperature. Such shifts have implications for global ocean circulation, Southern Ocean upwelling and productivity, and atmospheric CO_2 ^{1–3}. It is therefore paramount to consider the DO cycle from a global, rather than a purely North Atlantic, perspective.

Online content

Any methods, additional references, Nature Research reporting summaries, source data, statements of data availability and associated accession codes are available at <https://doi.org/10.1038/s41586-018-0727-5>.

Received: 11 May 2018; Accepted: 12 October 2018;
Published online 28 November 2018.

1. Marshall, J. & Speer, K. Closure of the meridional overturning circulation through Southern Ocean upwelling. *Nat. Geosci.* **5**, 171–180 (2012).
2. Toggweiler, J. R., Russell, J. L. & Carson, S. R. Midlatitude westerlies, atmospheric CO_2 , and climate change during the ice ages. *Paleoceanography* **21**, PA2005 (2006).

3. Biastoch, A., Boning, C. W., Schwarzkopf, F. U. & Lutjeharms, J. R. E. Increase in Agulhas leakage due to poleward shift of Southern Hemisphere westerlies. *Nature* **462**, 495–498 (2009).
4. Pritchard, H. D. et al. Antarctic ice-sheet loss driven by basal melting of ice shelves. *Nature* **484**, 502–505 (2012).
5. Lee, S. Y., Chiang, J. C., Matsumoto, K. & Tokos, K. S. Southern Ocean wind response to North Atlantic cooling and the rise in atmospheric CO₂: modeling perspective and paleoceanographic implications. *Paleoceanography* **26**, PA1214 (2011).
6. Pedro, J. B. et al. Beyond the bipolar seesaw: toward a process understanding of interhemispheric coupling. *Quat. Sci. Rev.* **192**, 27–46 (2018).
7. Schneider, T., Bischoff, T. & Haug, G. H. Migrations and dynamics of the intertropical convergence zone. *Nature* **513**, 45–53 (2014).
8. Markle, B. R. et al. Global atmospheric teleconnections during Dansgaard–Oeschger events. *Nat. Geosci.* **10**, 36–40 (2017).
9. Ding, Q., Steig, E. J., Battisti, D. S. & Kuttel, M. Winter warming in West Antarctica caused by central tropical Pacific warming. *Nat. Geosci.* **4**, 398–403 (2011).
10. Buiron, D. et al. Regional imprints of millennial variability during the MIS 3 period around Antarctica. *Quat. Sci. Rev.* **48**, 99–112 (2012).
11. Stocker, T. F. & Johnsen, S. J. A minimum thermodynamic model for the bipolar seesaw. *Paleoceanography* **18**, 1087 (2003); correction **20**, PA1002 (2005).
12. Rind, D. et al. Effects of glacial meltwater in the GISS coupled atmosphere–ocean model. 2. A bipolar seesaw in Atlantic Deep Water production. *J. Geophys. Res. Atmos.* **106**, 27355–27365 (2001).
13. Kostov, Y. et al. Fast and slow responses of Southern Ocean sea surface temperature to SAM in coupled climate models. *Clim. Dyn.* **48**, 1595–1609 (2017).
14. Jouzel, J. et al. Validity of the temperature reconstruction from water isotopes in ice cores. *J. Geophys. Res.* **102**, 26471–26487 (1997).
15. WAIS Divide Project Members. Precise interglacial phasing of abrupt climate change during the last ice age. *Nature* **520**, 661–665 (2015).
16. Merlivat, L. & Jouzel, J. Global climatic interpretation of the deuterium–oxygen 18 relationship for precipitation. *J. Geophys. Res.* **84**, 5029–5033 (1979).
17. Masson-Delmotte, V. et al. GRIP deuterium excess reveals rapid and orbital-scale changes in Greenland moisture origin. *Science* **309**, 118–121 (2005).
18. Masson-Delmotte, V. et al. Abrupt change of Antarctic moisture origin at the end of Termination II. *Proc. Natl Acad. Sci. USA* **107**, 12091–12094 (2010).
19. Schmidt, G. A., LeGrande, A. N. & Hoffmann, G. Water isotope expressions of intrinsic and forced variability in a coupled ocean–atmosphere model. *J. Geophys. Res.* **112**, D10103 (2007).
20. Uemura, R. et al. Ranges of moisture-source temperature estimated from Antarctic ice cores stable isotope records over glacial–interglacial cycles. *Clim. Past* **8**, 1109–1125 (2012).
21. Sodemann, H. & Stohl, A. Asymmetries in the moisture origin of Antarctic precipitation. *Geophys. Res. Lett.* **36**, L22803 (2009).
22. Lefebvre, W., Goosse, H., Timmermann, R. & Fichefet, T. Influence of the Southern Annular Mode on the sea ice–ocean system. *J. Geophys. Res.* **109**, C09005 (2004).
23. Thompson, D. W. J. & Wallace, J. M. Annular modes in the extratropical circulation. Part I: month-to-month variability. *J. Clim.* **13**, 1000–1016 (2000).
24. Sen Gupta, A. & England, M. H. Coupled ocean–atmosphere–ice response to variations in the Southern Annular Mode. *J. Clim.* **19**, 4457–4486 (2006).
25. Liu, Z. et al. Transient simulation of last deglaciation with a new mechanism for Bolling–Allerod warming. *Science* **325**, 310–314 (2009).
26. Ferreira, D., Marshall, J., Bitz, C. M., Solomon, S. & Plumb, A. Antarctic Ocean and sea ice response to ozone depletion: a two-time-scale problem. *J. Clim.* **28**, 1206–1226 (2015).
27. Raisbeck, G. M. et al. An improved north–south synchronization of ice core records around the 41 kyr ¹⁰Be peak. *Clim. Past* **13**, 217–229 (2017).
28. Grootes, P. M., Stuiver, M., White, J. W. C., Johnsen, S. & Jouzel, J. Comparison of oxygen isotope records from the GISP2 and GRIP Greenland ice cores. *Nature* **366**, 552–554 (1993).
29. Rhodes, R. H. et al. Enhanced tropical methane production in response to iceberg discharge in the North Atlantic. *Science* **348**, 1016–1019 (2015).
30. Dee, D. P. et al. The ERA-Interim reanalysis: configuration and performance of the data assimilation system. *Q. J. R. Meteorol. Soc.* **137**, 553–597 (2011).

Acknowledgements This work is funded by the US National Science Foundation (NSF), through grants ANT-1643394 (to C.B. and J.J.W.), ANT-1643355 (to T.J.F. and E.J.S.) and AGS-1502990 (to F.H.); the Swiss National Science Foundation through grant 200021_143436 (to H.S.); the CNRS/INSU/LEFE projects IceChrono and CO2Role (to F.P.); JSPS KAKENHI grants 15H01731 (to K.G.-A., H.M. and M.H.), 15KK0027 (to K.K.) and 26241011 (to K.K., S.F. and H.M.); MEXT KAKENHI grant 17H06320 (to K.K., H.M. and R.U.); the European Research Council under the European Community’s Seventh Framework Programme (FP7/2007–2013)/ERC grant agreement 610055 (to J.B.P.); and the NOAA Climate and Global Change Postdoctoral Fellowship programme, administered by the University Corporation for Atmospheric Research (F.H.). We acknowledge high-performance computing support from Yellowstone (ark:/85065/d7wd3xhc) provided by NCAR’s Computational and Information Systems Laboratory, sponsored by the NSF. This research used resources of the Oak Ridge Leadership Computing Facility at the Oak Ridge National Laboratory, which is supported by the Office of Science of the US Department of Energy under contract number DE-AC05-00OR22725. This is TALDICE publication number 52.

Reviewer information *Nature* thanks N. Abram, S. Davies and T. Stocker for their contribution to the peer review of this work.

Author contributions Data analysis by C.B., M. Severi, M. Sigl and J.J.W.; manuscript preparation by C.B.; volcanic ice-core synchronization by M. Sigl, M. Severi, C.B., J.R.M., F.P., S.F. and T.J.F.; GCM simulations and interpretation by F.H., J.B.P. and J.J.W.; moisture tagging/tracing experiments by B.R.M. and H.S.; ice-core water isotope analysis by K.G.-A., K.K., H.M., M.H., R.U., B.S. and E.J.S.; all authors discussed the results and contributed towards improving the final manuscript.

Competing interests The authors declare no competing interests.

Additional information

Extended data is available for this paper at <https://doi.org/10.1038/s41586-018-0727-5>.

Supplementary information is available for this paper at <https://doi.org/10.1038/s41586-018-0727-5>.

Reprints and permissions information is available at <http://www.nature.com/reprints>.

Correspondence and requests for materials should be addressed to C.B.

Publisher’s note: Springer Nature remains neutral with regard to jurisdictional claims in published maps and institutional affiliations.

METHODS

Volcanic ice-core synchronization. Volcanic reference horizons provide the most precise way to synchronize ice-core age scales^{31–35}. Within the last decade, progress has been made in volcanically linking the EDC ice core to the EDML core³¹, the TAL core³² and the DF core³⁵. Here we provide new volcanic stratigraphic links between the WDC and the EDML, EDC and TAL cores using pattern matching of volcanic peaks in high-resolution records of either sulfur (WDC) or sulfate (EDML, EDC and TAL). Extended Data Fig. 1b summarizes the various synchronizations, with previously published ones indicated with grey arrows and the new ones presented here indicated with coloured arrows.

Volcanic synchronization via sulfur, sulfate or electrical conductivity measurement (ECM) records is a commonly used technique for Antarctic ice cores, and we rely on previously established methods described in detail elsewhere^{31–35}. Matches are made by identifying sequences of sulfur peaks that have the same relative spacing in both cores^{31–33,35}. Additional confidence in the match points comes from approximately proportional acid-concentration levels, smooth variations in the resulting annual layer thickness between stratigraphic tie-points, and in some cases a distinctive shape of the common signals in the different ice cores. We identify 773 volcanic ties between WDC and EDML, 396 between WDC and EDC, and 425 between WDC and TAL (Supplementary Data).

Stratigraphic matching is performed independently by two of the authors (analyst 1 and analyst 2) and then compiled and compared by a third author. Both analysts use an iterative approach, in which they first identify the major, unambiguous events. After marking these events (or clusters thereof), they re-align the datasets and replot them with the marked events overlapping. At this point, usually several of the smaller events are nearly on top of each other. These events are then marked and the data are replotted with the newly marked events overlapping, and the process is repeated.

We distinguish three cases: ‘doubly’, ‘singly’ and ‘inconsistently’ identified events. Doubly identified matches are cases where both analysts identify the same stratigraphic match between two cores for a given volcanic event (within a margin of a few centimetres). Singly identified matches are cases where only one of the two analysts identifies a stratigraphic match. Inconsistently identified matches are cases where a single volcanic peak in one core is linked to two different volcanic peaks in the other core. Around 99% of the singly identified events are found by analyst 1, demonstrating a difference in event detection threshold. For example, in the WDC–EDC synchronization the median volcanic peak sizes in WDC non-sea-salt sulfur are 67.7 and 31.4 p.p.b. for the doubly and singly identified matches, respectively, demonstrating that analyst 2 is more conservative in assigning match points. For comparison, the background non-sea-salt sulfur level is 15 ± 4 p.p.b.

Here, all the doubly identified events are assumed to be correct and retained. In the (relatively rare) case of an inconsistently matched event, the stratigraphic links suggested by both analysts are discarded to avoid ambiguity. Sequences of singly identified events are retained only if they occur in between two doubly identified match points. In the case of an inconsistently identified event (which is discarded), all singly identified matches adjacent to it are discarded also, until another doubly identified match is encountered. We give some examples below of hypothetical sequences of tie points, and how they are dealt with. In the following, ‘d’, ‘s’ and ‘i’ denote doubly, singly and inconsistently identified tie points, respectively.

d–s–s–d. This is a hypothetical series of three **s** tie points between two **d** tie points. Because both analysts agree on the tie points on either end, there is no reason to assume that the **s** tie points are incorrect; it simply reflects the fact that analyst 2 is more conservative in assigning tie points than analyst 1. Therefore all tie points are retained in the final synchronization (**d–s–s–d**); **s** tie points are retained in such cases irrespective of how many are present in the series (for example, a series of ten **s** ties would be retained if bracketed on either side by a **d**).

d–i–d. In this case the **i** tie is removed, but the **d** ties are retained, resulting in the sequence **d–d** in the final synchronization.

d–s–i–s–d. The **i** tie is removed in all cases. However, in this example the **s** tie points occur adjacent to an **i** tie point, which casts doubt on their reliability. Therefore they are removed together with the inconsistent tie, and only the sequence **d–d** is retained in the final synchronization.

The matching is described here for the 10–61 kyr interval of interest (the WDC–EDC synchronization extends back only to 57 kyr BP). In synchronizing WDC and EDC, the two analysts identified 473 matches, out of which 103 were doubly, 8 were inconsistently and 362 were singly identified (all but two of which were identified by analyst 1). The final selection retained the 103 doubly identified matches and 293 of the singly identified matches; 69 singly identified matches were discarded because they were bracketed on either side by an inconsistent match. The 8 inconsistently identified matches all differed by less than 70 cm in EDC (or about 65 yr).

In synchronizing WDC and EDML, the two analysts identified a total of 793 matches, out of which 247 were doubly identified, 3 matches were inconsistently identified (all adjacent, and not separated by doubly identified events) and 543 were singly identified (all by analyst 1). The final selection retained the 247 doubly

identified matches and 526 of the singly identified matches; 17 singly identified matches were discarded because they were bracketed on either side by an inconsistent match. The 3 inconsistently identified matches all differed by less than 1.6 m in EDML (or about 65 yr).

TAL proved to be the most difficult of the cores to synchronize, presumably because the layers are more strongly compressed in this intermediate-depth core. The first attempt at synchronization yielded 55 doubly and 5 inconsistently identified matches, with most of the errors in the 770–905 m depth range (up to 5-m offsets in TAL). In light of this inconsistency, the analysts reviewed their volcanic ties throughout the core, with particular focus on the problematic interval. In the revised synchronization, the analysts identified a total of 437 matches, out of which 253 were doubly identified, 4 matches were inconsistently identified (all adjacent, and not separated by doubly identified events) and 180 were singly identified (all but 9 by analyst 1). The final selection retained the 253 doubly identified matches and 172 of the singly identified matches; 8 singly identified matches were discarded. The 4 inconsistently identified matches all differed by less than 75 cm in TAL (or about 75 yr). So while the final synchronization shows good agreement between the two analysts, we feel obliged to also report the first, less successful attempt. The TAL depth range that is hardest to synchronize to WDC (770–905 m TAL depth, or 14.9–25.2 kyr BP) also yielded no matches to EDC in a published study³² (see yellow triangles at the bottom of Extended Data Fig. 1a). We note that this problematic time interval of 15–25 kyr BP does not influence the main results of this work—none of the abrupt DO events used in the stacking lie in this interval (DO event 2 is excluded from the stacking because the absence of an abrupt CH₄ signal precludes precise synchronization to Greenland¹⁵).

The number of doubly and inconsistently identified events provides one way to assess the reliability of the volcanic synchronization; the percentage of inconsistently identified events (out of the pool of doubly and inconsistently identified events) ranges from 1% to 7% for the three cores. Errors tend to occur in clusters of adjacent picks owing to the misidentification of a sequence of peaks; seen in this light, each of the WDC–EDML and WDC–TAL synchronizations contains only a single inconsistently identified sequence. The observed inconsistencies are always relatively small and of the order of a few decades. A second method of assessing the reliability of the volcanic synchronization is via the redundancy offered by having multiple cores. Whenever three ice cores in Extended Data Fig. 1b are connected via three independent synchronizations (that is, whenever the arrows form a triangle), this offers the possibility to test the internal consistency of the synchronization. Over the age interval of interest (the last 61 kyr), 213 ties had been previously identified between EDML and EDC³⁶, as well as 102 ties between TAL and EDC. This introduces a degree of redundancy that allows testing the internal consistency of the synchronization. EDC, TAL and EDML are volcanically synchronized within the AICC2012 (Antarctic Ice Core Chronology)³⁶, whereas WDC uses the independent WD2014 timescale^{37,38}. For each volcanic tie point, the difference between the WD2014 age and the AICC2012 age is shown in Extended Data Fig. 1a. EDC and EDML are volcanically synchronized over the last 60 kyr (blue triangles), and therefore the excellent agreement between the blue (WDC age minus EDML age) and red (WDC age minus EDC age) curves in Extended Data Fig. 1a shows the volcanic framework to be internally consistent. Likewise, for the period 25–42 kyr BP and <13 kyr BP, where TAL and EDC are volcanically synchronized (yellow triangles), the yellow (WDC age minus TAL age) and red curves agree well, suggesting internal consistency. Beyond 42 kyr BP the yellow curve deviates from the blue and red ones, suggesting that the TAL core is imperfectly synchronized within the AICC2012 chronology (owing to an absence of volcanic ties at the time).

All ice cores used in this study were synchronized to the WD2014 chronology^{37,38}. For the four non-WDC cores, we start from their original ice-core chronologies; this is the AICC2012 chronology³⁶ for the EDML, EDC and TAL ice cores, and the DF2006 chronology for the DF core³⁹. For each core we add a time-variable offset to the WD2014 chronology that is obtained using linear interpolation between the volcanic tie points. For the EDML, EDC and TAL cores we have direct synchronizations to WDC as described above. For the DF core, synchronization is indirect via the EDC core (Extended Data Fig. 1b). Previously, 297 tie points had been identified³³ between EDC and DF in the interval of interest (mean spacing of 173 years). These volcanic ties are transferred to WDC using the WDC–EDC synchronization described above.

Over the time interval of interest, the offset of the AICC2012 cores (EDML, EDC and TAL) ranges roughly from –330 yr to +430 yr, with an average offset of –10 yr (with negative values meaning that WD2014 is younger than AICC2012). For the DF core the range is from –230 to 1,884 yr, with an average of +739 yr. **Uncertainty in volcanic synchronization.** There are two types of uncertainty to consider. First, the volcanic ties themselves may be incorrect; second, between ties the interpolation strategy introduces an error. The first type is difficult to quantify. Either the ties are correctly identified and the relative age uncertainty is zero, or the ties are false and the relative age uncertainty is infinite (that is, we have learned

nothing). Past studies have sometimes assigned Gaussian errors to volcanic tie points; although this is a practical necessity for applications that optimize the fit to multiple age constraints^{36,40–42}, it does not reflect the true uncertainty meaningfully and is not applied here.

We have high confidence in the correctness of the volcanic ties because of the internal consistency of the new volcanic ties with previously published ones (Extended Data Fig. 1a), and the fact that doubly identified ties greatly outnumber the inconsistently identified ones. We have removed inconsistent matches from the synchronization, and we assume the remaining matches to be correct.

The second type of uncertainty is due to interpolation between volcanic ties. This introduces an age uncertainty that depends on the age difference between adjacent ties, L . We estimate the interpolation uncertainty using the layer-counted section of the WD2014 chronology, which goes back to 31.2 kyr BP. To estimate the interpolation uncertainty for two volcanic markers that are, say, $L = 100$ yr apart, we can randomly pick thousands of 100-yr intervals from the WD2014 chronology. Within each of these, the age evolution deviates from the assumed linear interpolation, and 1σ of this age deviation is used as the interpolation uncertainty. Typical results are shown in Extended Data Fig. 2a for several values of L . We find that the maximum uncertainty scales as $\propto L^2$. Compared with East Antarctica, West Antarctica receives a larger contribution of its snowfall from storm systems and synoptic activity, making accumulation rates more variable^{43,44}; the estimates given here should thus be considered conservative when used in the interior of Antarctica. The volcanic interpolation uncertainty for the four cores is plotted in Extended Data Fig. 2b. For DF, synchronization to WDC is done using EDC as an intermediary core, and therefore the two synchronization errors are added in quadrature.

In our synchronization we use both the singly and doubly identified tie points and treat them equally. We acknowledge, however, that the doubly identified ties are more reliable. Therefore, we repeat the analyses described in the main text using only the doubly identified tie points (as opposed to both singly and doubly identified tie points) and we find that the conclusions of this work do not depend on this choice of tie points. Those tests are not shown here, but alternative chronologies that use only the doubly identified tie points and alternative versions of the manuscript figures showing those analyses are available from the corresponding author upon request.

Ice-core water stable-isotope data. A combination of previously published and unpublished ice-core water isotope data ($\delta^{18}\text{O}$ and δD ; where δD represents the $^2\text{H}/^1\text{H}$ composition) are used in this study. The deuterium excess (d_{in}) is calculated from the $\delta^{18}\text{O}$ and δD isotope ratios using the logarithmic definition of ref. 20:

$$d_{\text{in}} = \ln(1 + \delta\text{D}) - 8.47 \ln(1 + \delta^{18}\text{O}) + 0.0285 [\ln(1 + \delta^{18}\text{O})]^2$$

For WDC we use previously published $\delta^{18}\text{O}$ and δD data^{8,15,45} measured using laser spectroscopy. The data have a typical depth resolution of 1 m for the 0–2.3 kyr BP interval, of 0.5 m for 2.3–56 kyr BP and of 0.25 m for 56–68 kyr BP; this corresponds to an average time resolution of 17 yr for the study period (11–61 kyr BP). Using the centimetre-scale continuous-flow-analysis record of WDC $\delta^{18}\text{O}$ instead gives identical results to those presented here⁴⁶.

For EDML we use previously published $\delta^{18}\text{O}$ and δD data^{47,48} measured using conventional isotope ratio mass spectrometry (IRMS). The data have a typical depth resolution of 0.5 m, corresponding to an average time resolution of 24 yr for the study period.

For EDC we use previously published $\delta^{18}\text{O}$ and δD data^{48,49} measured using conventional IRMS. The data have a typical depth resolution of 0.55 m, corresponding to an average time resolution of 44 yr for the study period.

For DF we use new and published water isotope data^{39,50,51}. Two datasets are used. The first contains $\delta^{18}\text{O}$ data measured using IRMS in the 300–1,151 m depth range (10–71 kyr BP) at 0.5-m resolution⁵⁰. The second is a set of $\delta^{18}\text{O}$ and δD data measured using IRMS in the 550–849 m depth range (23–45 kyr BP); this dataset was measured at 0.1-m resolution and averaged into 0.5-m bins. We note that d_{in} is only available from the second dataset, which spans DO events 2–11 (DO event numbering is shown in Fig. 1). In the depth range of overlap, $\delta^{18}\text{O}$ data from both datasets are averaged (after correcting the second dataset by +0.213‰ to account for a calibration offset) to produce the final time series. The combined $\delta^{18}\text{O}$ record has an average time resolution of 35 yr for the study period.

For TAL we use a combination of new and previously published^{10,52,53} data. Bag-average, 1-m resolution $\delta^{18}\text{O}$ and δD data measured using IRMS are available for the entire core. High-resolution (0.1 m) $\delta^{18}\text{O}$ data measured using IRMS are available in the 598–786 m (10–16 kyr BP) and 1,030–1,282 m (37–65 kyr BP) depth ranges. High-resolution $\delta^{18}\text{O}$ data are averaged into 0.5-m bins and combined with bag-average data for the remaining depth intervals. The combined $\delta^{18}\text{O}$ record has an average time resolution of 50 yr for the study period.

Stacking procedure. The stacking procedure used to investigate the Antarctic climate response to abrupt DO variability is described in detail elsewhere¹⁵.

In short, the individual Greenland events are aligned at the midpoint of their abrupt $\delta^{18}\text{O}$ transitions (either DO warming or DO cooling). All Antarctic events (on their volcanically synchronized WD2014 timescales) are aligned at the midpoints of the abrupt WDC CH_4 transitions. We then average over events to obtain the shared climatic signal; to derive the north–south phasing we use the independently established CH_4 delay of 56 ± 19 yr (1σ) behind $\delta^{18}\text{O}$ in Greenland⁵⁴.

For one of the abrupt events (DO 10), improved inter-polar synchronization data are available from ^{10}Be variations during the Laschamp event (41 kyr BP) between the Greenland NGRIP core and the Antarctic EDC and EDML cores²⁷; these timing constraints are incorporated into our stacking procedure (DO 10 only). The EDML, EDC, DF and TAL ice cores have CH_4 records with much higher (gas age–ice age) difference (Δage) uncertainty and lower resolution than WDC, therefore the north–south phasing precision cannot be improved by considering CH_4 synchronization for those cores also.

In this work we consider DO 0 (that is, the Younger Dryas–Holocene transition) through DO 16; DO 17 falls outside the volcanic synchronization for the EDC and DF cores. DO 2 is omitted owing to the absence of a clear CH_4 response, precluding synchronization. All stacked records are shown in Extended Data Fig. 3.

Uncertainty in the timing of the stacked records comes from the following sources: (1) the Δage in the WDC core²⁷; (2) DO midpoint detection in the abrupt NGRIP $\delta^{18}\text{O}$ record; (3) DO midpoint detection in the abrupt WDC CH_4 record; (4) interpolation of the WDC chronology between tie points; (5) the climatic lag of 56 ± 19 yr (1σ) of atmospheric CH_4 behind Greenland $\delta^{18}\text{O}$ ⁵⁴; (6) trend analysis in the BREAKFIT⁵⁵ and RAMPFIT⁵⁶ fitting routines; and (7) volcanic synchronization to the WD2014 chronology.

The combined uncertainty due to the first five items was assessed previously using a Monte Carlo routine, suggesting a 1σ timing uncertainty of 38 yr and 41 yr in the WDC stacks for DO warming and DO cooling, respectively¹⁵. The uncertainty in the trend analysis is given in Extended Data Table 1. The uncertainty in the volcanic synchronization is shown in Extended Data Fig. 2; averaged over the stacked events, the 1σ synchronization uncertainty is 0 yr at WDC, 2 yr at EDML, 6 yr at EDC, 13 yr at DF and 2 yr at TAL.

By stacking only the most prominent DO events (those following Heinrich events; that is, DO events 0, 1, 4, 8, 12 and 14) or just the minor ones (the remainder), we find that the magnitude of the atmospherically forced Antarctic response is larger for the former, suggesting proportionality with the climate perturbation (Extended Data Fig. 4a–f). Proportionality of the atmospheric response is further seen for individual events (Extended Data Fig. 4g; see the figure legend for details). **PCA.** PCA allows different climatic modes to be identified in (palaeoclimatic) time series from different locations⁵⁷. Here we perform PCA on the stacked $\delta^{18}\text{O}$ records at the five individual sites using the MATLAB function *pca*. The $\delta^{18}\text{O}$ stacks discussed in the main text combine 19 individual events—all those that fall within the volcanic synchronization interval. To assess the sensitivity of our conclusions to including or excluding individual events, we perform additional experiments in which we stack only n events (rather than all 19). The n events are randomly sampled without replacement (that is, any given event cannot be picked twice for each stacking). We then perform PCA of these stacked records (the same events are stacked for each of the cores) and standardize the principal component vectors by taking the z -score (or standard score). Extended Data Fig. 5 shows typical results for $n = 2$ and $n = 8$, where for each n we repeat the experiment 50,000 times to obtain reliable statistics. Extended Data Fig. 5a, b shows PC1 and PC2, respectively, with the solid line showing the mean of 50,000 experiments and the shaded envelope the associated $\pm 1\sigma$. Extended Data Fig. 5c shows a histogram of the percentage of variance explained by each of the modes.

We find that even by stacking as few as just $n = 2$ events, the method can, on average, identify the oceanic and atmospheric components described in the main text. Perhaps not surprisingly, we find that when including fewer events the signal-to-noise ratio decreases: with fewer events the estimated signal amplitude is smaller in both PC1 and PC2, and the uncertainty envelope is wider. As more events are included in the stacking, the percentage of variance explained by PC1 increases as the coherence between the various Antarctic cores increases owing to the improved signal-to-noise ratio.

The analysis discussed in the main text uses a 1,500-yr window (centred around $t = 100$ yr), which is chosen because it corresponds to the recurrence time of the shortest DO cycles^{58–61}. The variance explained by the oceanic and atmospheric modes depends on the window length, as shown in Extended Data Fig. 6a. For window lengths exceeding about 750 yr, the oceanic mode explains most of the variance (PC1), with the atmospheric mode explaining less. However, at short window lengths (<750 yr) the atmospheric mode explains most of the variance, making it PC1. The comparison of PC1 at a 400-yr window with PC2 at a 2,000-yr window (Extended Data Fig. 6b) illustrates the ability of the PCA to identify the atmospheric mode at different window lengths. The crossover behaviour (that is, the atmospheric mode shifts from being PC2 to being PC1 as a function of window length) is due to the fact that the signal variance of the step-like atmospheric mode

occurs chiefly within the $t=0$ to $t=100$ yr interval; signal variance of the oceanic mode depends strongly on the window length owing to its gradual nature.

Lag-time analysis of PC1 and PC2 using the RAMPFIT⁵⁶ and BREAKFIT⁵⁵ routines confirms the crossover behaviour. At short window lengths (<700 yr), PC1 is characterized by the instantaneous or fast response of the hypothesized atmospheric teleconnection, whereas at large window lengths (>800 yr) it shows the hypothesized 200-yr delayed oceanic teleconnection. PC2 shows the opposite behaviour; however, we note that for PC2 at a 400-yr window length no meaningful solution can be found with either routine. At window lengths >700 yr the lag times remain stable and vary only within the uncertainty bound. Unless specified otherwise, a 1,500-yr window is used in this work.

Robustness of the atmospheric spatial pattern. The spatial pattern that we identify for the atmospheric mode is one of the main results of this work, and we here test its robustness. In Extended Data Fig. 6d–f we compare three alternative ways of identifying the spatial pattern; the Pearson correlation coefficient (r) between the shown pattern and the pattern identified in the main text (EOF2 at a 1,500-yr window) is given for each. Details on the three methods are given in the figure legend. Correlation coefficients ranging from $r=0.92$ to $r=0.999$ suggest that identification of the atmospheric pattern is both qualitatively and quantitatively robust.

Rotated PCA vectors. PCA aims to explain the largest amount of variance, whereas our goal is to distinguish between the oceanic and atmospheric modes. While PC1 is clearly dominated by the 200-yr-delayed oceanic bipolar seesaw (Fig. 2d), it appears that PC1 also captures some abrupt warming around $t=0$, apparently because atmospherically induced warming is more prevalent over Antarctica than cooling (Northern Hemisphere DO warming case). We therefore construct (admittedly somewhat subjective) oceanic and atmospheric response functions (Fig. 2e), which are derived from the principal components in the following way. Let PC1 and PC2 be the first two principal components through time; these vectors are perpendicular. We let the atmospheric response, *ATM*, be identical to PC2. The oceanic response, *OCE*, is found by rotating the PC1 vector in the plane spanned by vectors PC1 and PC2 over an angle of -13° :

$$OCE = \cos(-13^\circ)PC1 + \sin(-13^\circ)PC2$$

The rotation angle of -13° is picked such that the $\delta^{18}O$ shift at $t=0$ is minimized. The spatial pattern associated with *ATM* (Fig. 2h) is found by multiple linear regression of the $\delta^{18}O$ stacks at the individual sites to *OCE* and *ATM* using the MATLAB function *regress*.

SAM, PSA and synthetic ‘atmospheric’ indices. The SAM and PSA indices are calculated from climate-model and reanalysis data as the first and second mode of variability, respectively, in the PCA/EOF analysis (MATLAB function *pca*) of the sea-level pressure (model) or the 850-hPa geopotential height (reanalysis) south of 20° S, after subtracting the long-term mean and scaling the anomalies by the square root of the cosine of the latitude to account for the decreased surface area closer to the poles. A synthetic index of the inferred atmospheric teleconnection is created by projecting the reanalysis SAT anomalies at the ice-core locations onto the atmospheric loading coefficients from Fig. 2h, the spatial signature of which is shown in Fig. 4d. Mathematically, this projection is done by multiplying the SAT anomalies with the loading coefficients and summing over them at each monthly time step.

It is worth noting that all these inferences with respect to reanalysis data rely upon just five atmospheric loading coefficients from the limited (from the perspective of large-scale circulation) spatial domain of Antarctica, so it is difficult to rigorously exclude non-SAM atmospheric influences from the temperature pattern alone.

In Extended Data Fig. 9 we compare the variability in the Southern Hemisphere westerly winds calculated with glacial CCSM3 climate simulations^{25,62} with that obtained from the ERA-Interim reanalysis³⁰. Both results show greater variability in the Indian and Pacific sectors than in the Atlantic sector. Compared to ERA-Interim, the CCSM3 SAM is more zonal/annular in its structure; the CCSM3 westerlies also appear to have smaller variability (some of this difference could be due to comparing annual mean with decadal mean data). In CCSM3 the forced response of the Southern Hemisphere westerlies (at 19 kyr BP, in response to increased North Atlantic freshwater; right panel) is very similar to the internal variability of the Southern Hemisphere westerlies (middle panel), suggesting that the change in the Southern Hemisphere atmospheric circulation induced by freshwater forcing in the North Atlantic is analogous to the existing mode of internal variability.

To estimate the magnitude of SAM shifts of the DO cycle, we analyse the changes in central East Antarctica, where the signal is the largest and most consistent with the observed present-day relationship (Fig. 4). Using an isotope sensitivity of $0.8\% K^{-1}$, the atmospherically induced temperature anomaly in central East Antarctica (DF, EDC) is in the range 0.20 – $0.45^\circ C$ during DO warming (the lower and upper bounds reflect typical minor and major DO events, respectively). Regression of the ERA-Interim 2-m temperature at DF and EDC to the SAM index

shows a slope of around $-1.2^\circ C$ per unit of normalized SAM (the normalized SAM index time series has a standard deviation of 1), implying a shift in the SAM index of around 0.2 to 0.4 normalized (modern-day) SAM units (rounded to one significant figure). This estimate assumes: (1) a linear isotope–temperature response using the modern-day spatial slope, and (2) that the monthly SAM–SAT regression from the monthly internal SAM variability also applies to persistent SAM shifts during the glacial DO cycle; both assumptions are subject to uncertainties that we do not address here. The CCSM3 model simulates a persisting SAM shift of the same magnitude as the internal SAM variability in decadal averaged data (Fig. 3); because internal SAM variability will be larger in monthly than in decadal averaged data, the model and database estimates may be in agreement. The reanalysis time period is too short to derive robust estimates of decadal averaged SAM variability.

GCM simulations. We analyse previously published TraCE-21k transient climate model simulations with CCSM3^{25,62–65}. AMOC collapse and resumption are triggered using freshwater forcing in the North Atlantic. The ‘DGL19k’ run is used for the AMOC collapse and the ‘DGL-overshoot-C’ run for the AMOC resumption case⁶⁴.

Moisture origin analysis. We use two separate experiments to trace the moisture origin of the precipitation at the coring sites. The first method uses a Lagrangian moisture source diagnostic⁶⁶ based on a previously published dataset⁶⁷. Using the winds, temperature and humidity of the ERA-Interim reanalysis dataset³⁰ covering the years 1980–2013, we calculate 5 million air parcel trajectories covering the global atmosphere at a resolution of 6 h using the Lagrangian particle dispersion model FLEXPART⁶⁸. From the analysis of specific humidity changes over time along the air parcel trajectories, moisture sources are identified whenever the specific humidity in the air parcels increases more than a threshold value of $0.1 g kg^{-1}$ over a 6-h period. The fractional contribution of each moisture source to the final precipitation at the target location (an area of $300 \times 300 km^2$ centred on each ice-core site) is obtained from calculating the amount contributed by a moisture source to the humidity already present in an air parcel. For precipitation en route, the contributions of previous sources are proportionally discounted. This results in a quantitative estimate of the contribution of surface areas to the precipitation in the target region in units of evaporation (water mass per unit area per unit time), including their position (latitude and longitude). The moisture source contributions for each site and precipitation event are combined into mass-weighted annual mean values and scaled with respect to the total amount of water deposited at the target region.

The second method uses water tagging in a 50-yr simulation with the Community Atmosphere Model (CAM) with prescribed seasonally varying SST and modern boundary conditions. The experiment is set up to evaluate the meridional moisture source distribution, with further details and figures given in ref. ⁸. In short, evaporation is tagged in 11 bins. One bin is the Antarctic continent (re-evaporation) and the ocean and ice shelves south of $70^\circ S$; the other ten bins are zonal bins of 5° latitude each, ranging from $20^\circ S$ to $70^\circ S$. For each core, the moisture source distribution is found by evaluating the relative contributions from each of the bins for the last 30 years of the run. Two moisture source distributions are created, one for all years in which the mean annual SAM index was positive, and one for all years in which it was negative (Extended Data Fig. 8b).

Change-point detection. We use two well documented and widely used change-point detection methods, BREAKFIT⁵⁵ and RAMPFIT⁵⁶, with the results given in Extended Data Table 1. The choice of method is based on the shape of the time series $x(t)$. BREAKFIT finds a single change point and fits a linear slope on either side; these features make it suitable for the oceanic mode/PC1 discussed in the main manuscript. RAMPFIT finds two change points; it assumes that $x(t)$ has a constant value x_1 for $t < t_1$, then is ramped up or down until it reaches value x_2 at time t_2 , after which it remains constant at value x_2 for $t > t_2$. These features make RAMPFIT suitable for the atmospheric mode/PC2 discussed in the main manuscript. To find the two change points in the d_{in} stacks, we apply both the RAMPFIT and the BREAKFIT algorithms twice (once for each change point). The results are comparable (Extended Data Table 1), and in the main text we report the average of the two methods.

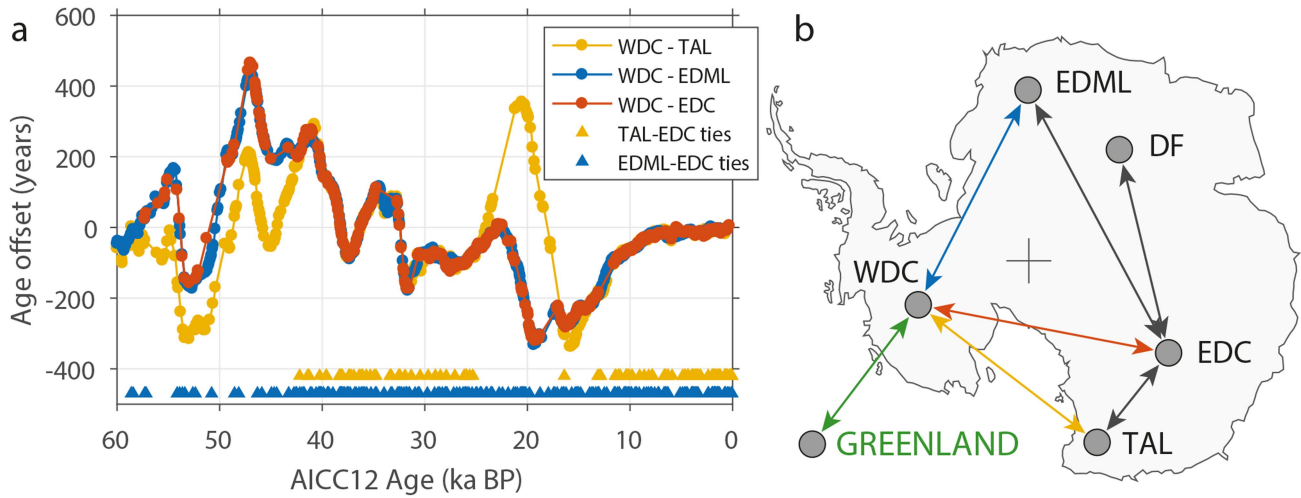
Code availability. The MATLAB code used for the stacking procedure can be found in the supplementary information of ref. ¹⁵ and is available from the corresponding author upon request.

Data availability

Source Data (WDC sulfur data, volcanic tie points and water isotope data on synchronized chronologies) and derived products (stacks, PCA results, etc.) are available in the online version of the paper and in the NOAA palaeoclimate data archive.

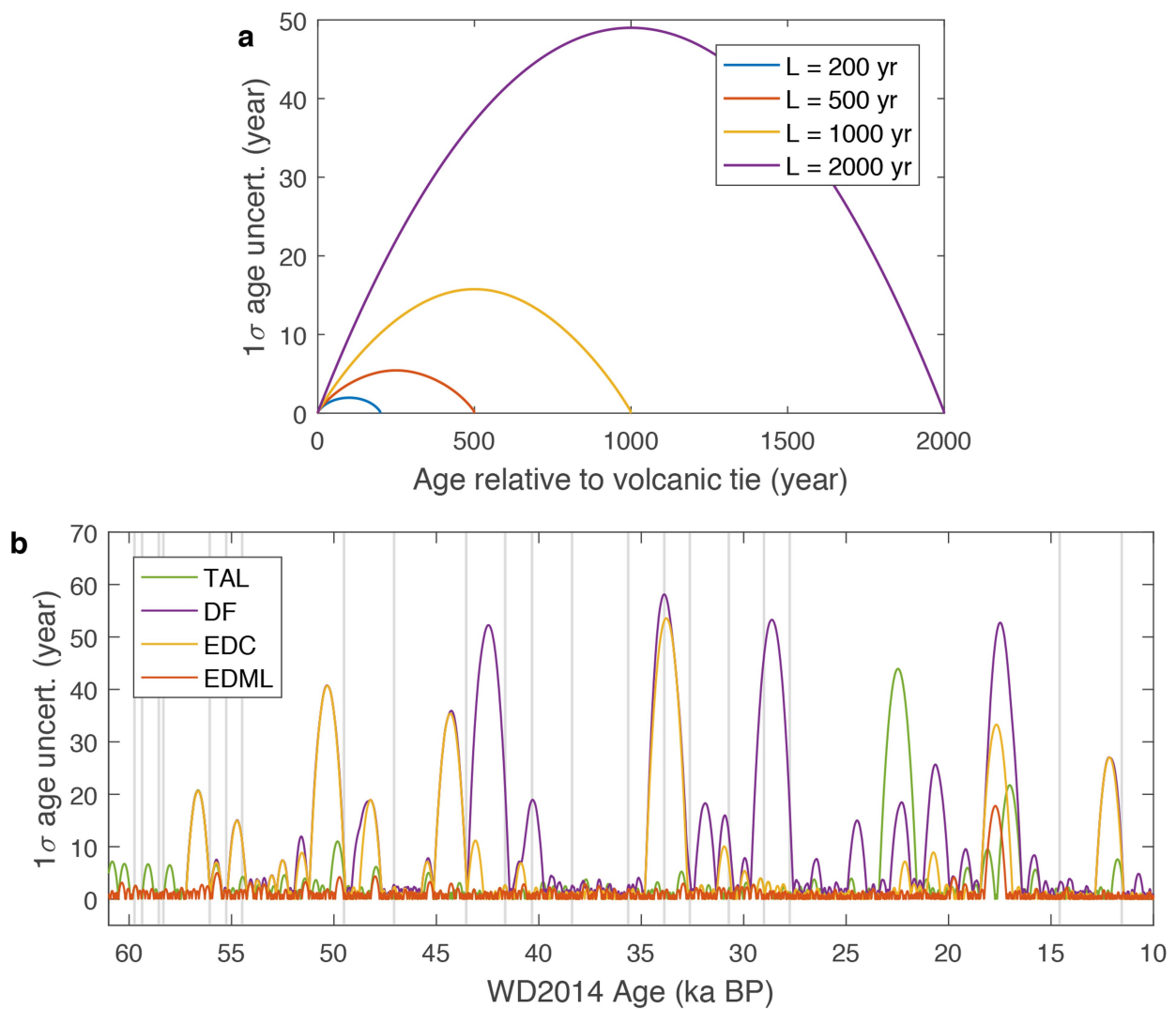
31. Severi, M. et al. Synchronisation of the EDML and EDC ice cores for the last 52 kyr by volcanic signature matching. *Clim. Past* **3**, 367–374 (2007).

32. Severi, M., Udisti, R., Becagli, S., Stenni, B. & Traversi, R. Volcanic synchronisation of the EPICA-DC and TALDICE ice cores for the last 42 kyr BP. *Clim. Past* **8**, 509–517 (2012).
33. Fujita, S., Parrenin, F., Severi, M., Motoyama, H. & Wolff, E. W. Volcanic synchronization of Dome Fuji and Dome C Antarctic deep ice cores over the past 216 kyr. *Clim. Past* **11**, 1395–1416 (2015).
34. Sigl, M. et al. Insights from Antarctica on volcanic forcing during the Common Era. *Nat. Clim. Chang.* **4**, 693–697 (2014).
35. Parrenin, F. et al. Volcanic synchronisation between the EPICA Dome C and Vostok ice cores (Antarctica) 0–145 kyr BP. *Clim. Past* **8**, 1031–1045 (2012).
36. Veres, D. et al. The Antarctic ice core chronology (AICC2012): an optimized multi-parameter and multi-site dating approach for the last 120 thousand years. *Clim. Past* **9**, 1733–1748 (2013).
37. Buizert, C. et al. The WAIS Divide deep ice core WD2014 chronology – part 1: methane synchronization (68–31 ka BP) and the gas age–ice age difference. *Clim. Past* **11**, 153–173 (2015).
38. Sigl, M. et al. The WAIS Divide deep ice core WD2014 chronology – part 2: annual-layer counting (0–31 ka BP). *Clim. Past* **12**, 769–786 (2016).
39. Kawamura, K. et al. Northern Hemisphere forcing of climatic cycles in Antarctica over the past 360,000 years. *Nature* **448**, 912–916 (2007).
40. Bazin, L. et al. An optimized multi-proxy, multi-site Antarctic ice and gas orbital chronology (AICC2012): 120–800 ka. *Clim. Past* **9**, 1715–1731 (2013).
41. Parrenin, F. et al. IceChrono1: a probabilistic model to compute a common and optimal chronology for several ice cores. *Geosci. Model Dev.* **8**, 1473–1492 (2015).
42. Lemieux-Dudon, B. et al. Consistent dating for Antarctic and Greenland ice cores. *Quat. Sci. Rev.* **29**, 8–20 (2010).
43. Fudge, T. J. et al. Variable relationship between accumulation and temperature in West Antarctica for the past 31,000 years. *Geophys. Res. Lett.* **43**, 3795–3803 (2016).
44. Fortuin, J. & Oerlemans, J. Parameterization of the annual surface temperature and mass balance of Antarctica. *Ann. Glaciol.* **14**, 78–84 (1990).
45. WAIS Divide Project Members. Onset of deglacial warming in West Antarctica driven by local orbital forcing. *Nature* **500**, 440–444 (2013).
46. Jones, T. R. et al. Water isotope diffusion in the WAIS Divide ice core during the Holocene and last glacial. *J. Geophys. Res. Earth* **122**, 290–309 (2017).
47. EPICA Community Members. One-to-one coupling of glacial climate variability in Greenland and Antarctica. *Nature* **444**, 195–198 (2006).
48. Stenni, B. et al. The deuterium excess records of EPICA Dome C and Dronning Maud Land ice cores (East Antarctica). *Quat. Sci. Rev.* **29**, 146–159 (2010).
49. Jouzel, J. et al. Orbital and millennial Antarctic climate variability over the past 800,000 years. *Science* **317**, 793–796 (2007).
50. Kawamura, K. et al. State dependence of climatic instability over the past 720,000 years from Antarctic ice cores and climate modeling. *Sci. Adv.* **3**, (2017).
51. Uemura, R. et al. Asynchrony between Antarctic temperature and CO₂ associated with obliquity over the past 720,000 years. *Nat. Commun.* **9**, 961 (2018).
52. Stenni, B. et al. Expression of the bipolar see-saw in Antarctic climate records during the last deglaciation. *Nat. Geosci.* **4**, 46–49 (2011).
53. Landais, A. et al. A review of the bipolar see-saw from synchronized and high resolution ice core water stable isotope records from Greenland and East Antarctica. *Quat. Sci. Rev.* **114**, 18–32 (2015).
54. Baumgartner, M. et al. NGRIP CH₄ concentration from 120 to 10 kyr before present and its relation to a $\delta^{15}\text{N}$ temperature reconstruction from the same ice core. *Clim. Past* **10**, 903–920 (2014).
55. Mudelsee, M. Break function regression. *Eur. Phys. J. Spec. Top.* **174**, 49–63 (2009).
56. Mudelsee, M. Ramp function regression: a tool for quantifying climate transitions. *Comput. Geosci.* **26**, 293–307 (2000).
57. Clark, P. U., Pisias, N. G., Stocker, T. F. & Weaver, A. J. The role of the thermohaline circulation in abrupt climate change. *Nature* **415**, 863–869 (2002).
58. Grootes, P. M. & Stuiver, M. Oxygen 18/16 variability in Greenland snow and ice with 10⁻³-to-10⁵-year time resolution. *J. Geophys. Res.* **102**, 26455–26470 (1997).
59. Alley, R. B., Anandakrishnan, S. & Jung, P. Stochastic resonance in the North Atlantic. *Paleoceanography* **16**, 190–198 (2001).
60. Buizert, C. & Schmittner, A. Southern Ocean control of glacial AMOC stability and Dansgaard-Oeschger interstadial duration. *Paleoceanography* **30**, 1595–1612 (2015).
61. Ditlevsen, P. D., Kristensen, M. S. & Andersen, K. K. The recurrence time of Dansgaard-Oeschger events and limits on the possible periodic component. *J. Clim.* **18**, 2594–2603 (2005).
62. He, F. et al. Northern Hemisphere forcing of Southern Hemisphere climate during the last deglaciation. *Nature* **494**, 81–85 (2013).
63. Liu, Z. et al. Younger Dryas cooling and the Greenland climate response to CO₂. *Proc. Natl Acad. Sci.* **109**, 11101–11104 (2012).
64. He, F. Simulating Transient Climate Evolution of the Last Deglaciation with CCSM3. PhD thesis, Univ. Wisconsin-Madison (2010).
65. Pedro, J. B. et al. The spatial extent and dynamics of the Antarctic Cold Reversal. *Nat. Geosci.* **9**, 51–55 (2016).
66. Sodemann, H., Schwierz, C. & Wernli, H. Interannual variability of Greenland winter precipitation sources: Lagrangian moisture diagnostic and North Atlantic Oscillation influence. *J. Geophys. Res.* **113**, D03107 (2008).
67. Läderach, A. & Sodemann, H. A revised picture of the atmospheric moisture residence time. *Geophys. Res. Lett.* **43**, 924–933 (2016).
68. Stohl, A., Forster, C., Frank, A., Seibert, P. & Wotawa, G. Technical note: The Lagrangian particle dispersion model FLEXPART version 6.2. *Atmos. Chem. Phys.* **5**, 2461–2474 (2005).
69. Locarnini, R. A. et al. *World Ocean Atlas 2013, Volume 1: Temperature* (eds Levitus, S. & Mishonov, A.) (NOAA/NESDIS, Silver Spring, 2013).
70. Kalnay, E. et al. The NCEP/NCAR 40-year reanalysis project. *Bull. Am. Meteorol. Soc.* **77**, 437–471 (1996).



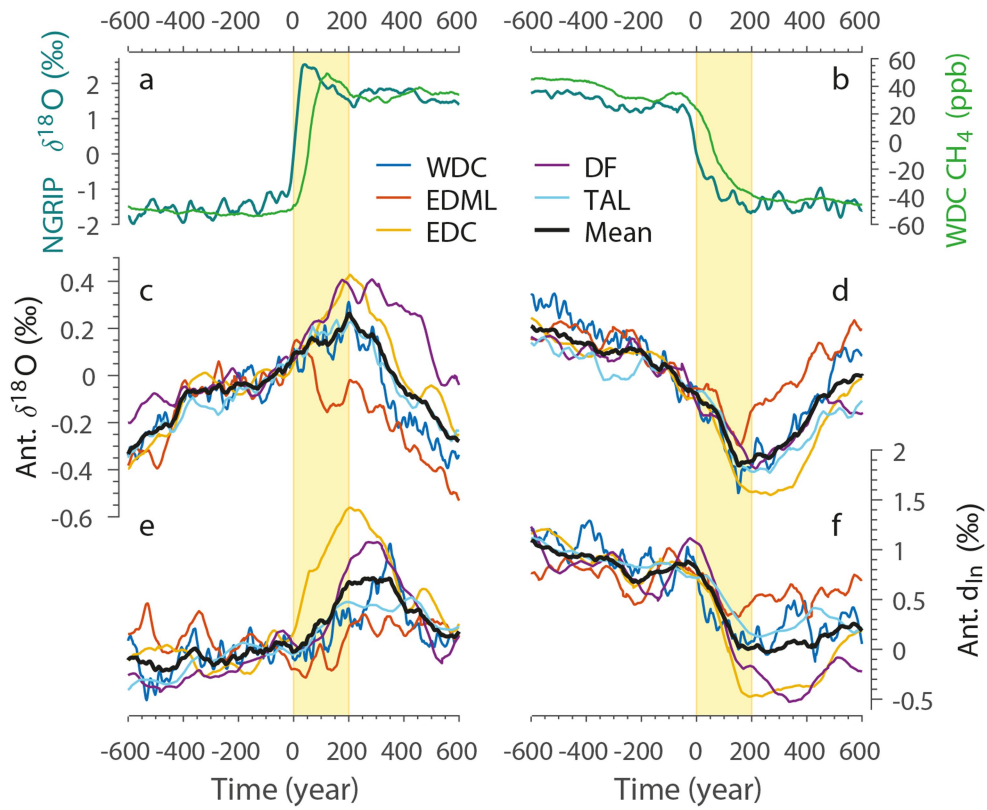
Extended Data Fig. 1 | Volcanic synchronization of Antarctic ice cores. **a**, Age offset between the WD2014^{37,38} (WDC) and AICC2012³⁶ (TAL, EDML, EDC) age scales, with each dot representing a volcanic tie point. Yellow and blue triangles denote the timing of TAL-EDC and EDML-EDC volcanic ties^{32,36}, respectively. **b**, Overview of synchronizations

between the ice cores used in this study. Grey arrows indicate previously published synchronizations and coloured arrows denote synchronizations performed here. Synchronizations within Antarctica are based purely on volcanic links; synchronization between WDC and NGRIP (Greenland) are based on atmospheric CH₄ (green arrow).



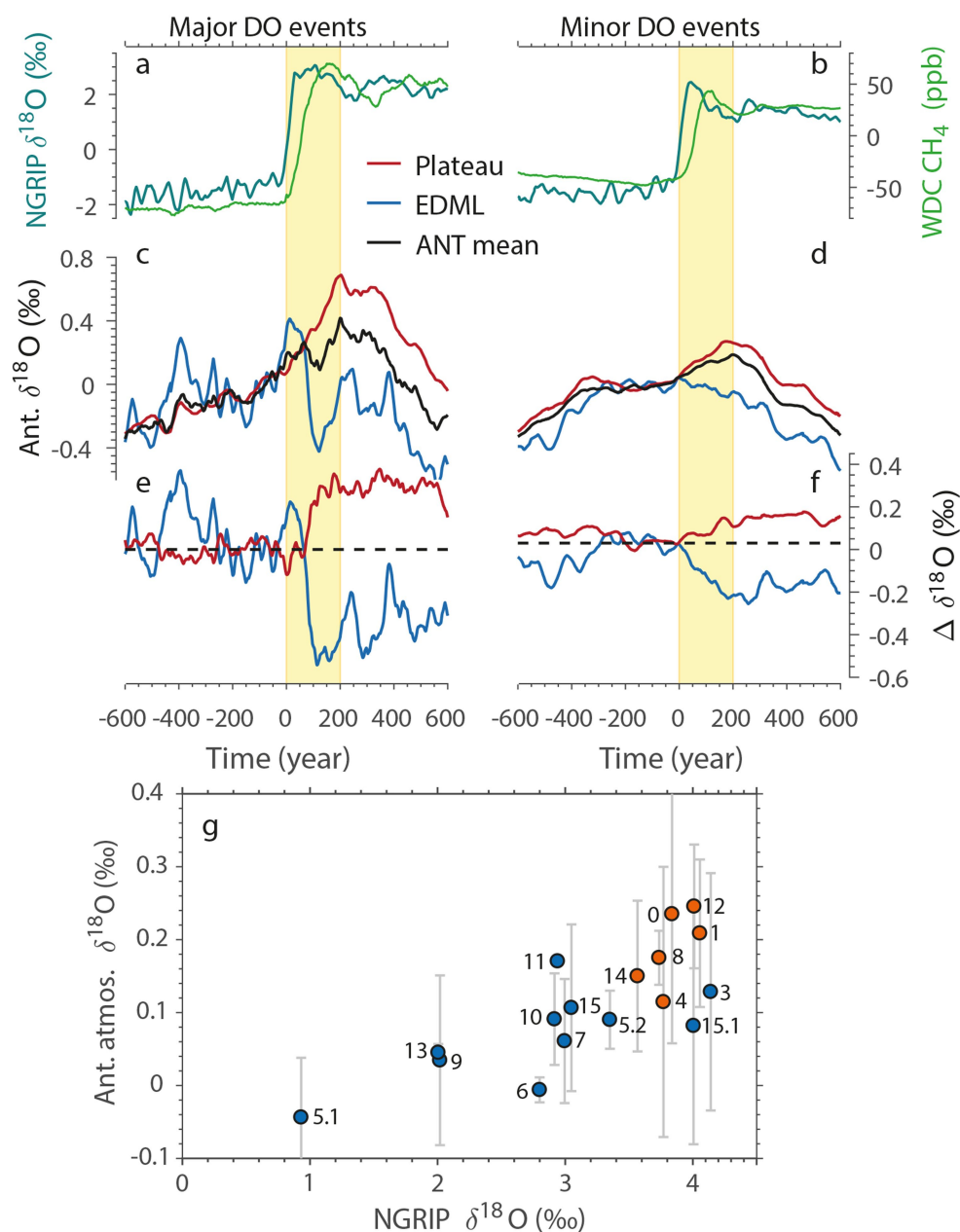
Extended Data Fig. 2 | Age uncertainty due to volcanic synchronization. **a**, Interpolation uncertainty (1σ) for four different values of L (the spacing between two adjacent volcanic tie points), based on the layer-counted

WD2014 age scale³⁸. **b**, Interpolation uncertainty in synchronizing the four ice cores to WD2014 chronology. Grey vertical lines give the timing of DO events.



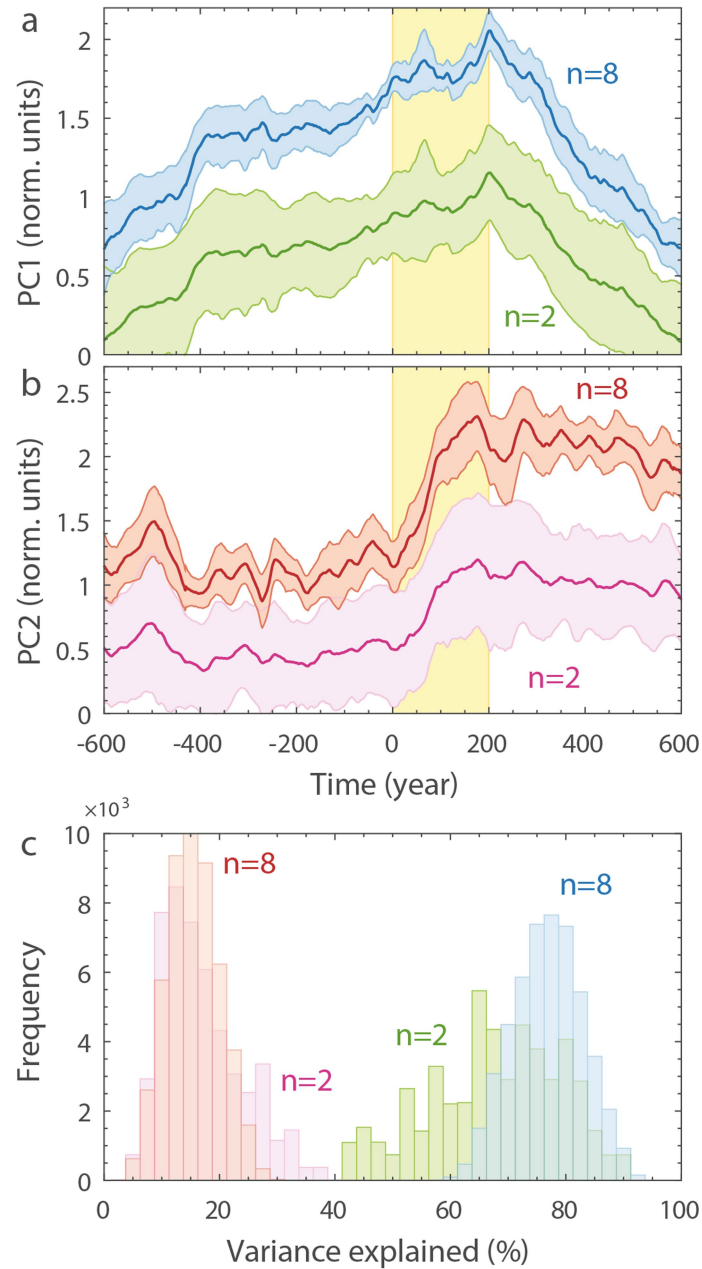
Extended Data Fig. 3 | Site-specific stacks of $\delta^{18}\text{O}$ and d_{1n} . **a**, Stack of NGRIP $\delta^{18}\text{O}$ (teal; left axis) and WDC CH_4 (green; right axis) during DO warming. **b**, As in **a**, but for DO cooling. **c**, Stack of Antarctic $\delta^{18}\text{O}$ at the indicated locations (see key) during DO warming. **d**, As in **c**, but for DO

cooling. **e**, Stack of Antarctic d_{1n} at the indicated locations during DO warming. **f**, As in **e**, but for DO cooling. Isotope ratios are on the VSMOW scale.



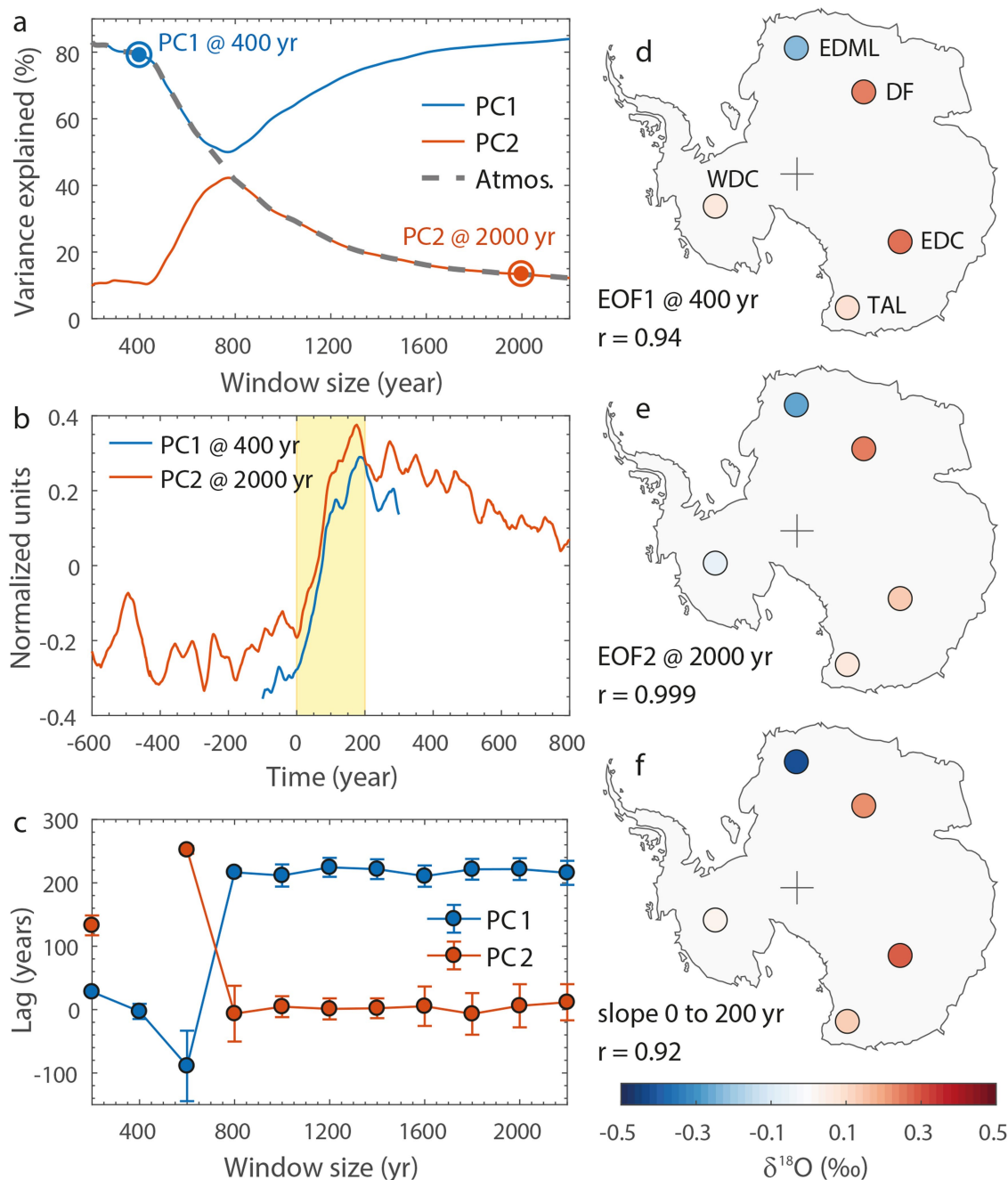
Extended Data Fig. 4 | Proportionality of the atmospheric response. **a–f**, Comparison of stacks of just the major DO events (those following Heinrich events, namely, DO events 0, 1, 4, 8, 12 and 14; **a**, **c**, **e**) and just the minor DO events (the remainder; **b**, **d**, **f**). **a**, **b**, Stacks of NGRIP $\delta^{18}\text{O}$ (left axis) and CH_4 (right axis). **c**, **d**, Stacks of Antarctic $\delta^{18}\text{O}$ at the indicated locations. **e**, **f**, As in **c** and **d**, but with the Antarctic mean subtracted. **g**, Proportionality of the atmospheric response for individual events (numbered). The NGRIP event size is found via regression of individual NGRIP events to the multi-event NGRIP $\delta^{18}\text{O}$ stack normalized

to unit variance (Fig. 2a). The Antarctic atmospheric response is found via multiple linear regression of single-site individual events to the atmospheric and oceanic modes (Fig. 2e). Shown are the average (dots) and standard deviation (error bars) of the response at EDC, DF and EDML (the cores with the strongest atmospheric response); the EDML response is multiplied by -1 because it has the opposite sign of the response at DF and EDC. Red and blue dots denote the major and minor DO events, respectively. Isotope ratios are on the VSMOW scale.



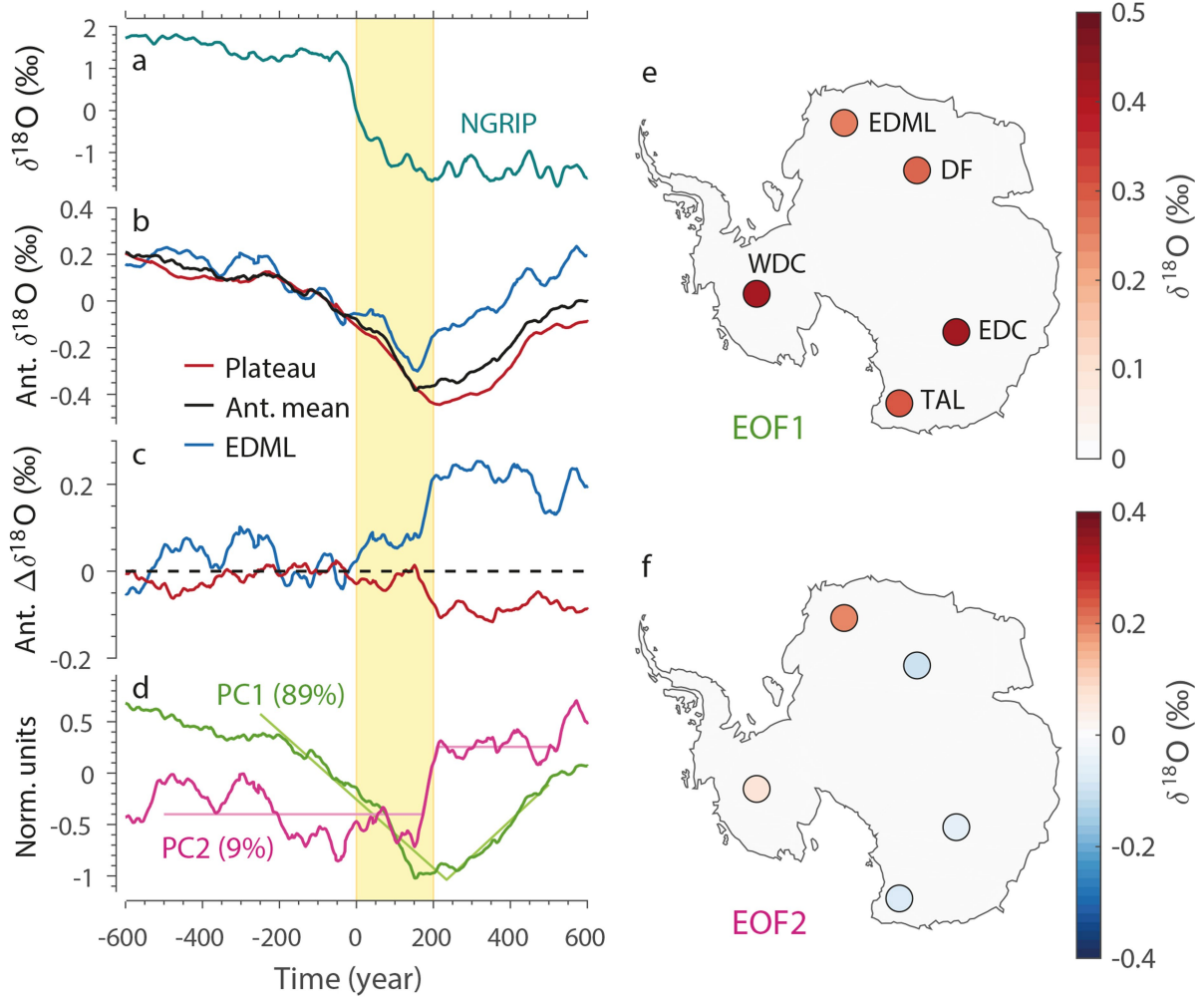
Extended Data Fig. 5 | Reduction of the number of events in the $\delta^{18}\text{O}$ stacks. **a**, PC1, when stacking $n=2$ and $n=8$ randomly selected events. The thick line and shaded area represent the mean and $\pm 1\sigma$, respectively, obtained from 50,000 runs. The vertical yellow bands denote the 200-yr

period after the abrupt DO event at $t=0$. **b**, As in **a**, but for PC2. **c**, Fraction of signal variance explained by PC1 and PC2, when stacking 2 or 8 randomly selected events. Colour coding as in **a** and **b**.



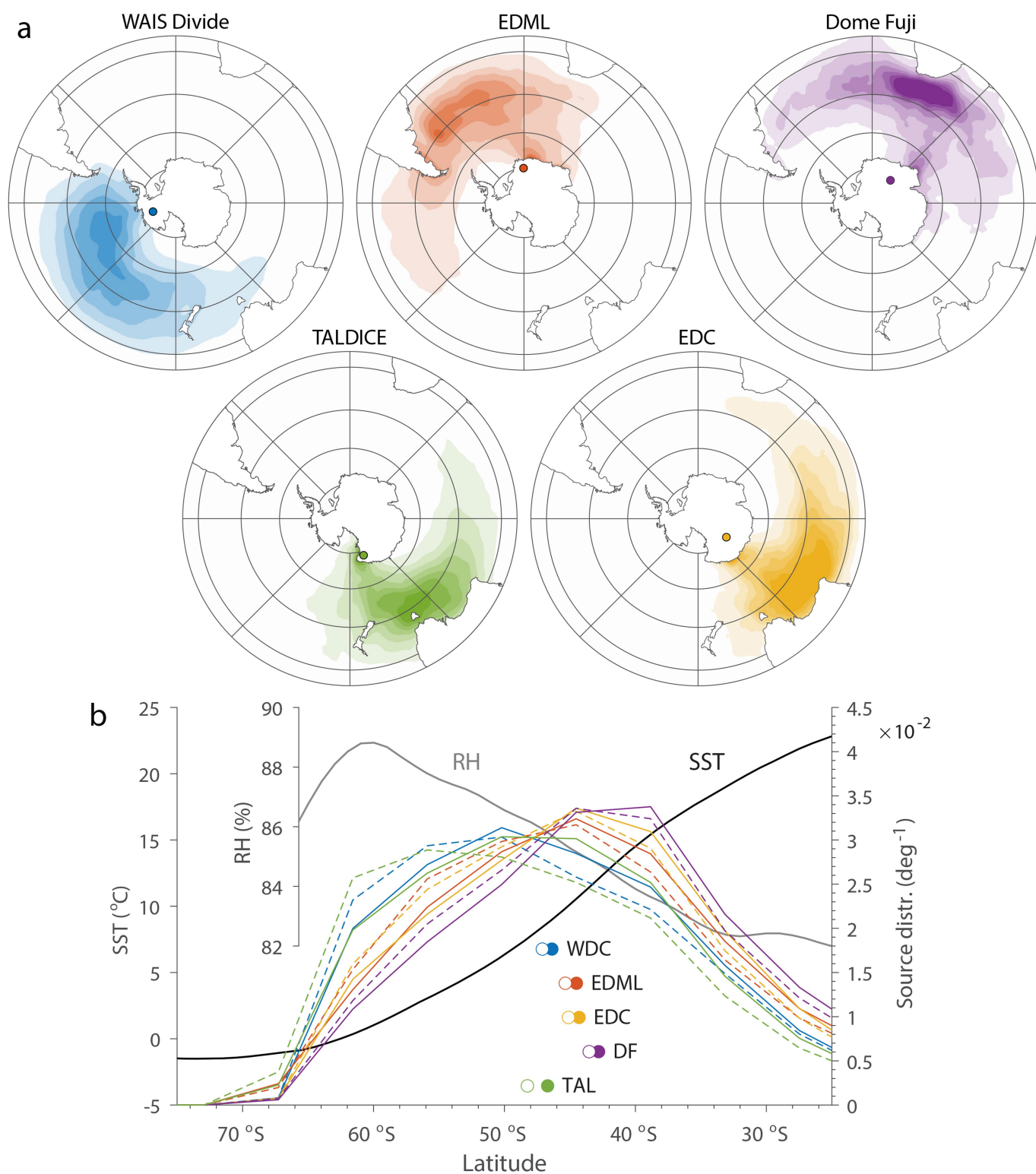
Extended Data Fig. 6 | Robustness of the atmospherically forced warming pattern. **a**, PCA as a function of window length, with the fraction of variance explained by PC1 and PC2. **b**, Comparison of PC1 at a 400-yr window length to PC2 at a 2,000-yr window length, showing the crossover of the atmospheric response (that is, from PC1 to PC2) as a function of window length. **c**, Lag time of the Antarctic PC1 and PC2 response as a function of window length, assessed using the BREAKFIT⁵⁵

and RAMPFIT⁵⁶ routines (see Methods for the selection of routine). **d**, EOF1 at a 400-yr window length, expressed in units of $\delta^{18}\text{O}$ (‰). **e**, EOF2 at a 2,000-yr window length, expressed in units of $\delta^{18}\text{O}$ (‰). **f**, Slope of linear fit to $\delta^{18}\text{O}$ stacks in the interval $t = 0$ to $t = +200$ yr, shown as the change (in ‰) during these 200 years. Isotope ratios are on the VSMOW scale.



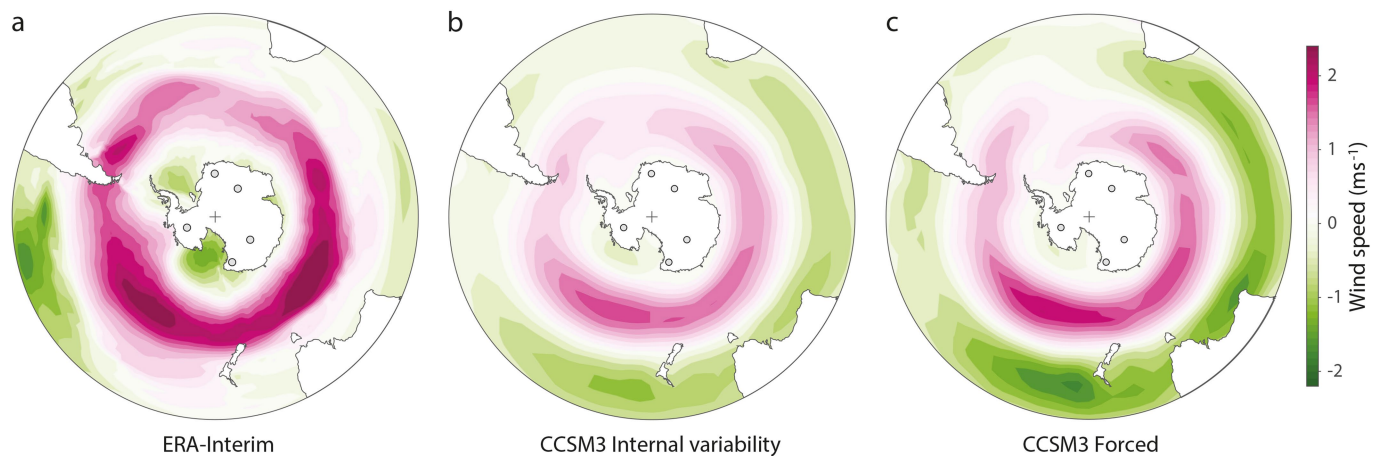
Extended Data Fig. 7 | Antarctic climate response to DO cooling.
a, Stack of NGRIP $\delta^{18}\text{O}$. **b**, Stack of Antarctic $\delta^{18}\text{O}$ at indicated locations.
c, As in **b**, but with the Antarctic mean subtracted. **d**, First two principal components of the Antarctic $\delta^{18}\text{O}$ stacks, with the fraction of variance

explained (offset for clarity). The lines show the BREAKFIT (PC1) and RAMPFIT (PC2) fits. **e**, **f**, Empirical orthogonal functions EOF1 and EOF2 associated with PC1 and PC2 in **d**, scaled to show the magnitude in units of $\delta^{18}\text{O}$ (‰). Isotope ratios are on the VSMOW scale.



Extended Data Fig. 8 | Moisture sources of Antarctic ice cores and the SAM. **a**, Mass-weighted probability distribution functions of Antarctic moisture sources for the five ice cores of interest ($5 \times 10^{-5} \text{ deg}^{-2}$ contour lines; the area-integrated probability distribution function equals 1). Distributions are calculated from reanalysis data^{30,67} using a Lagrangian source diagnostic^{21,66} (Methods). Parallels are plotted in 15° increments of latitude and meridians in 45° increments of longitude. **b**, SST (black)⁶⁹ and relative humidity (RH; grey)⁷⁰ as a function of latitude. The coloured

curves give the latitudinal source distribution during a negative SAM phase (solid curves; SAM index < 0) and a positive SAM phase (dashed curves; SAM index > 0). The solid and open dots show the first moment of the source distribution during negative and positive SAM phases, respectively. We note that during a positive SAM phase, moisture sources for all core locations are located closer to the Antarctic continent. Source distribution data were obtained using water tagging experiments⁸ in the CAM (Methods).



Extended Data Fig. 9 | SAM-like variability in zonal near-surface winds. **a**, ERA-Interim reanalysis (1979–2016 annual means) zonal wind speed at a height of 10 m, regressed onto the SAM index (here the first principal component of sea-level pressure variability south of 20° S), expressed in metres per second per standard deviation in the index. **b**, As in **a**, but for internal variability in the CCSM3 TraCE model simulation^{25,62} during

glacial climate before freshwater forcing of Heinrich stadial 1 (19.5 kyr BP to 19.01 kyr BP, decadal means). **c**, As in **a**, but for the response to North Atlantic freshwater forcing in the CCSM3 TraCE model (19.1 kyr BP to 18.9 kyr BP, decadal means, with the freshwater forcing applied at 19 kyr BP).

Extended Data Table 1 | Change-point analysis of Antarctic response

Parameter	Response to:	t_{OCE}	t_{ATM1}	t_{ATM2}	Routine:
$\delta^{18}\text{O}$ stack	DO warming	226 ± 23			BREAKFIT
$\delta^{18}\text{O}$ PC1	DO warming	222 ± 24			BREAKFIT
$\delta^{18}\text{O}$ ocean	DO warming	211 ± 12			BREAKFIT
$\delta^{18}\text{O}$ stack	DO cooling	225 ± 19			BREAKFIT
$\delta^{18}\text{O}$ PC1	DO cooling	234 ± 21			BREAKFIT
$\delta^{18}\text{O}$ PC2	DO warming		28 ± 3	137 ± 3	RAMPFIT
$\delta^{18}\text{O}$ atmos	DO warming		28 ± 3	137 ± 3	RAMPFIT
d_{in} stack	DO warming		-11 ± 34	193 ± 27	RAMPFIT
d_{in} stack	DO warming		28 ± 14	248 ± 14	BREAKFIT (2×)
CCSM3 SAM	DO warming		13 ± 38	68 ± 48	RAMPFIT
$\delta^{18}\text{O}$ PC2	DO cooling		171 ± 5	209 ± 5	RAMPFIT
d_{in} stack	DO cooling		6 ± 16	151 ± 19	RAMPFIT
d_{in} stack	DO cooling		12 ± 5	166 ± 6	BREAKFIT (2×)
CCSM3 SAM	DO cooling		20 ± 28	81 ± 29	RAMPFIT

Change points are found using the BREAKFIT⁵⁵ or RAMPFIT⁵⁶ routine, as indicated. The parameter t_{OCE} is the single change point of the oceanic mode; t_{ATM1} and t_{ATM2} are the two change points of the atmospheric mode, representing the onset and ending of the shift, respectively (Methods). Stated uncertainties give the 1σ value in the fitting routine only, found using a Monte Carlo moving-block bootstrap analysis with 1,000 iterations^{55,56}; the full uncertainty in the combined interpolator CH_4 synchronization and stacking procedure¹⁵ is estimated to be around 40 yr (1σ), which can mostly be attributed to uncertainty in the WAIS Divide ice age–gas age difference, Δage ³⁷. The $\delta^{18}\text{O}$ PC2 and $\delta^{18}\text{O}$ atmospheric modes are identical.